Microtubules form by progressively faster tubulin accretion, not by nucleation-elongation

Luke M. Rice[1], Michelle Moritz[2], David A. Agard[2]

[1] Departments of Biophysics and Biochemistry, UT Southwestern Medical Center, 5323 Harry Hines Blvd., Dallas TX 75390

[2] Department of Biochemistry and Biophysics, UC San Francisco, 600 16th St., San Francisco CA 94143

Correspondence: Luke.Rice@UTSouthwestern.edu, Agard@msg.ucsf.edu

Abstract

Microtubules are dynamic polymers that play fundamental roles in all eukaryotes. Despite their importance, how new microtubules form is poorly understood. Textbooks have focused on variations of a nucleation-elongation mechanism in which monomers rapidly equilibrate with an unstable oligomer (nucleus) that limits the rate of polymer formation; once formed, the polymer then elongates efficiently from this nucleus by monomer addition. Such models faithfully describe actin assembly, but they fail to account for how more complex polymers like hollow microtubules assemble. Here we articulate a new model for microtubule formation that has three key features: i) microtubules initiate via rectangular, sheet-like structures which grow faster the larger they become; ii) the dominant pathway proceeds via accretion, stepwise addition of longitudinal or lateral layers; iii) a 'straightening penalty' to account for the energetic cost of tubulin's curved-to-straight conformational transition. This model can quantitatively fit experimental assembly data, providing new insights into biochemical determinants and assembly pathways for microtubule nucleation.

Introduction

The microtubule cytoskeleton plays essential roles organizing the interior of eukaryotic cells: microtubules can act as “tracks” for motor-based transport, they form the basis of the mitotic spindle that mediates proper segregation of chromosomes during cell division, they help define cell polarization, and more (Barlan and Gelfand, 2017; Desai and Mitchison, 1997; Prosser and Pelletier, 2017). To fulfill these many roles, microtubules must assemble into a multitude of highly dynamic and spatially diverse networks. The dynamic instability of microtubules (Mitchison and Kirschner, 1984), which describes the switching of individual polymers between phases of growing and shrinking, allows wholesale reorganization of the microtubule network to occur rapidly and also provides a mechanism to efficiently search space (Holy and Leibler, 1994). Indeed, numerous regulatory factors allow cells to control how fast microtubules grow and how frequently they switch from growing to shrinking (catastrophe) or from shrinking back to growing (rescue) (Akhmanova and Steinmetz, 2015), and also to control the creation of new microtubules (Kollman et al., 2011; Roostalu and Surrey, 2017; Wieczorek et al., 2015), a process called nucleation.

Microtubules are hollow, cylindrical polymers formed from αβ-tubulin heterodimers that interact with each other in two ways: stronger head-to-tail (longitudinal) interactions between αβ-tubulins make up the straight protofilaments, and weaker side-to-side (lateral) interactions hold protofilaments together. The mechanisms underlying the dynamic instability of existing microtubules are increasingly well understood (Alushin et al., 2014; Driver et al., 2017; Duellberg et al., 2016; Gardner et al., 2011; Geyer et al., 2015; Grishchuk et al., 2005; Manka and Moores, 2018; Margolin et al., 2012; Piedra et al., 2016; VanBuren et al., 2005; VanBuren et al., 2002; Zhang et al., 2015), but models for how *existing* microtubules grow and shrink cannot specify how *new* microtubules form de novo. Thus, our understanding of the mechanisms that govern spontaneous microtubule formation remains relatively primitive (reviewed in

(Roostalu and Surrey, 2017)). Multiple factors contribute to this difficulty: first, nucleation occurs very rarely and cannot truly be observed microscopically, so measuring it directly is much harder than measuring the growing and shrinking of existing microtubules. Second, the open, tube-like structure of the microtubule poses unique complications. In most organisms, microtubules contain 13 protofilaments, although there are clear examples of specialized microtubules containing 11 or 15 protofilaments (Burton et al., 1975; Chaaban et al., 2018; Chalfie and Thomson, 1982; Davis and Gull, 1983; Kwiatkowska et al., 2006; Saito and Hama, 1982; Tucker et al., 1992). Regardless of protofilament number, the hollow nature of the microtubule means that it takes many more $\alpha\beta$-tubulin subunits to close a tube than it does to make a minimal helical repeat for a simpler, helical polymer like actin. Perhaps not surprisingly given this complexity, there is no consensus about the sequence of intermediates that must be formed (pathway) during the transition from individual subunits to a closed tube. To further complicate matters, the structure of the free heterodimer also changes during assembly, from a bent confirmation in solution to a straight conformation within the final microtubule ((Ayaz et al., 2012; Nawrotek et al., 2011; Rice et al., 2008); reviewed in (Brouhard and Rice, 2018)). Where in the assembly process the straightening takes place, whether it is continuous or step-wise, how much energy is required, and how this obligatory conformational change affects nucleation all remain unknown. In addition to these factors, the GTPase activity required for microtubule catastrophe can also antagonize nucleation by destabilizing intermediate species.

An early study of the kinetics of spontaneous microtubule nucleation, which used solution conditions that suppress catastrophe to simplify the behavior, posited that nucleation proceeded sequentially through two discrete intermediates (Voter and Erickson, 1984). The data were re-analyzed in later studies (Flyvbjerg et al., 1996; Kuchnir Fygenson et al., 1995) that proposed a more complex pathway containing four distinct nucleation intermediates (6-mer, 9-mer, 12-mer, and 15-

mer of αβ-tubulin). However, in this later analysis it was not possible to ascribe a biochemical interpretation to the species or rate constants (Flyvbjerg et al., 1996). Thus, the physical-chemical details of the underlying assembly process continue to remain obscure.

In this work, we sought to obtain more explicit insight into the molecular mechanisms that govern spontaneous microtubule assembly. Our primary goal was to explore the simplest biochemical models that could faithfully explain the experimental data. We began from the fundamental modes of αβ-tubulin interactions within a microtubule: a single subunit (heterodimer) can make a longitudinal interaction, a lateral interaction or make both simultaneously (corner interaction). Starting with explicit simulations of the biochemical reactions that can occur for all possible αβ-tubulin oligomers up to 12-mers, we observed that a small subset of all possible oligomers became dominant. These dominant oligomers were “rectangular”, meaning that they maximized the number of longitudinal and lateral contacts such that there were no unfilled corners. The dominance of a small subset of species allowed us to develop a simpler, approximate model based almost exclusively on rectangular oligomers. This simplification allowed the model to access arbitrarily large oligomers in a way that retained a connection to the fundamental biochemical interaction modes of the individual subunits.

This approximate but biochemically faithful model provides a new way to view microtubule nucleation. Rather than proceeding via a distinct rare, rate limiting “nucleus”, the model indicates that microtubule assembly involves the continuous accretion of αβ-tubulins into a growing 2D lattice. Like crystallization processes, the larger the assembly, the faster it grows. Our model reveals assembly pathways for forming a new microtubule and provides new insights into how exogeneous nucleators and other regulatory factors can accelerate microtubule formation.

Results

Rectangular species dominate the assembly pathway

To obtain biochemical insight into possible pathways for spontaneous microtubule assembly, we constructed an explicit model that includes all non-redundant tubulin oligomers from dimers through dodecamers (Fig. 1A shows the intermediates through hexamers). Here non-redundant means that we only consider a single exemplar N-mer for each unique combination of longitudinal and lateral contacts; statistical weighting of rate constants ensures that this exemplar oligomer faithfully represents the ensemble of species it represents (see example in Sup. Fig. 1). We defined the biochemical pathways that connect different oligomers (arrows in Fig. 1A) by assuming that oligomers grow and shrink via addition and loss of individual $\alpha\beta$-tubulin subunits. It was not practical to explore larger oligomers in this formulation because of an explosion in the number of species and reactions (reaching dodecamers requires ~200 distinct species and ~600 reactions) (Fig. 1F).

We implemented the differential equations describing this discrete assembly scheme in Berkeley Madonna (Marcoline et al., 2020) to simulate the assembly pathway and kinetics. The only free parameters in this model are the on rate constant k_f and the affinities for the three different $\alpha\beta$–tubulin interaction modes (longitudinal, lateral, and corner (simultaneous longitudinal+lateral interaction (Fig 1D). As is common, k_f was assumed (here we chose 10^6 $M^{-1}s^{-1}$ based on experimental observations and consistent with work from others (Coombes et al., 2013; Margolin et al., 2012; McIntosh et al., 2018; VanBuren et al., 2002; Zakharov et al., 2015)). We explored different values for the three parameters, seeking to identify conditions under which some appreciable concentration of dodecamers would form. We were especially interested in the corner affinity,

because this is the interaction that would provide the driving force for microtubule elongation. A relatively tight corner affinity ($K_d^{corner} < 0.2\ \mu M$; Sup. Fig. 2) was required for appreciable flux into the largest oligomers. With high-affinity corner interactions, the simulations predominantly populated a small number of 'rectangular' oligomers, defined as oligomers wherein (i) every subunit makes at least one longitudinal and one lateral contact to another, and (ii) there are no 'open' corner sites (Fig. 1B). More explicitly, what happens in the simulations is that formation of an initial 2x2 oligomer forms relatively quickly. The next larger species containing an additional 'singleton' tubulin are poorly populated because of the weak longitudinal and lateral affinities, but those species also present an open, high-affinity corner site. Filling this open site stabilizes the first subunit and in the case of a 2x2 start, fills the next longitudinal or lateral layer resulting in a 3x2 or 2x3 assembly, respectively. On larger assemblies, additional corners are vacant after the first, and these fill rapidly, essentially "zipping up" the layer. The net consequence is that once initiated, layer completion occurs efficiently, explaining why rectangular species dominate.

Only considering rectangular oligomers greatly reduces the number of species and reactions required to reach much larger oligomers in simulations (e.g. Fig. 1C,F). However, in such an approximation the rates of adding or losing a layer become context dependent, and depend on the height and width of the oligomer. Using the steady-state approximation, we were able to derive a general recursive expression for the effective 'forward' rate of adding of a longitudinal or lateral layer (see Methods). An example of adding a longitudinal layer to a 2x2 oligomer is illustrated in Fig. 1D. Considering the layer addition as a sequence of individual steps also allowed us to derive an effective forward rate as well as a 'layer equilibrium ratio', which describes the expected relative populations of oligomers that differ by a single layer (Methods). Importantly, in these expressions both the forward rate and equilibrium ratio for layer addition are defined in terms of the biochemical properties of individual subunits (longitudinal, lateral and corner

184 affinities/rates). Consequently, and in contrast to what occurs with
185 phenomenological models, the reduction in the number of species and reactions
186 does not come at the expense of losing a connection to the fundamental
187 biochemical behavior. For the 12-mer simulated explicitly above, the layer model
188 provides a >10-fold reduction in species and >35-fold reduction in number of
189 reactions (Fig. 1F) (these reduction factors increase dramatically for larger
190 oligomer sizes).
191
192 We implemented the reduced, layer-based model into Berkeley Madonna to test
193 if it could recapitulate the results from our explicit simulations when using the
194 same input parameters for subunit affinities. Despite the dramatic reduction in
195 complexity, and with the exception of very low-abundance intermediate species,
196 the simplified layer-based simulations quantitatively reproduced the oligomer
197 concentrations and the kinetics of oligomer formation observed with the explicit
198 model (compare Fig. 1E to 1B). These initial benchmarking layer simulations only
199 considered oligomers up to dodecamers so that we could make a direct
200 comparison with the explicit model. In the next section, we expand the model to
201 include the much larger oligomers required to depict microtubule assembly.
202
203 **A simplified accretion pathway for spontaneous microtubule assembly**
204 We wrote a custom program to expand the layer model to arbitrary sized
205 rectangular oligomers. Whenever an oligomer gained a 13th protofilament, we
206 converted it into a microtubule. No additional penalty for seam formation was
207 included. We assumed that once formed, microtubules elongate by capturing αβ-
208 tubulin subunits one at a time in the open, pseudo-helical 'corner' sites on either
209 end. In order to minimize the number of adjustable parameters, the same rate
210 constants were used for events at either the plus- or minus-ends. These
211 additional simplifying assumptions allow the model to simulate spontaneous
212 microtubule assembly and the ensuing depletion of free αβ-tubulin subunitsin a

213 relatively natural way, without having to explicitly specify a particular nucleus or
214 assume a preferred assembly pathway.
215
216 We began testing our model by fitting it to experimental assembly curves that we
217 measured by light scattering (Fig. 2A). The model was able to fit individual curves
218 quite well (Fig. 2B), with minor discrepancies evident at low concentration. The
219 optimized affinities differed somewhat from fit to fit, but shared common features:
220 tight corner affinities (K_d^{corn} < 100 nM), weaker longitudinal affinities (K_d^{long} ~5-15
221 mM), and lateral affinities around 10-fold weaker than longitudinal affinities (Fig.
222 2B). The longitudinal affinity we obtained is in the range of that obtained from
223 biochemical models for microtubule growing and shrinking (e.g.(Gardner et al.,
224 2011; Kim and Rice, 2019; Piedra et al., 2016; VanBuren et al., 2002)). The
225 corner and lateral affinities are both about 10-fold stronger than in those models,
226 a difference that might reflect the different buffer conditions (high glycerol
227 concentration) in 'nucleation' assays relative to 'dynamics' assays. The corner
228 affinity is much stronger than the product of longitudinal and lateral affinities,
229 which is expected because the individual longitudinal and lateral affinities
230 represent a balance between (among other things) favorable protein:protein
231 contacts and the unfavorable entropic cost of losing rotational and translational
232 degrees of freedom -- when making a corner interaction the longitudinal and
233 lateral interfaces both contribute favorably while the entropic cost remains
234 approximately the same (see also (Erickson and Pantaloni, 1981)). Fits to an
235 independent set of assembly curves (Sup. Fig. 3A) yielded similar affinities (Sup.
236 Fig. 3B). We found it encouraging that the model could fit individual assembly
237 curves, but to be convincing a single parameter set should be able to fit all the
238 assembly curves simultaneously. Thus, we turned to global fitting where we
239 attempted to fit the set of assembly curves with one common parameter set.
240
241 In a global fit to the set of assembly curves (Fig. 2C), a limitation of the model
242 became apparent: even though each individual concentration could be well fit

243 (Fig. 2B), the model could not capture the correct behavior over the broad
244 concentration range measured (Fig. 2C). The model appeared to fit the
245 alternative dataset somewhat better (Sup. Fig. 3C), but it was still apparent that
246 the model was underestimating the concentration-dependence of the assembly
247 curves; an outlier curve also limited the concentration range available for fitting.
248 Because all layer transition rates scale with the chosen on-rate constant (see
249 derivations in Methods), changing the assumed on-rate does not improve the
250 global fits. The observed discrepancy between model and experiment suggests
251 that the model fails to capture some important aspect of assembly. In re-
252 examining our assumptions, we realized that it was too restrictive to consider
253 only monomer addition and loss as the 'elemental' reactions within the layer
254 assembly pathway. Indeed, a simple calculation demonstrates that any model
255 having these relative lateral and longitudinal affinities must also include a 'dimer
256 pathway' (Fig. 2D). Compared to the 'two step' monomer-based pathway in
257 which a first monomer associates weakly and only becomes 'locked in' by a
258 subsequent corner association (Fig. 2D, middle path), when the longitudinal
259 affinity is stronger than the lateral one as it is for microtubules it is more efficient
260 to initiate a lateral layer by adding a pre-formed longitudinal dimer (Fig. 2D, lower
261 path). This is true even though longitudinal dimers are present at very low
262 concentrations (roughly 1 part in a 1000 or ~10 nM) for the parameters we used.
263 Our 'monomer only' model global fit required a longitudinal affinity ~10-fold
264 stronger than the lateral one, but under those conditions additions of longitudinal
265 dimers should actually account for ~90% of the lateral layer initiations (Fig. 2E).
266 Thus, despite appearing reasonable, the fits do not make biochemical sense
267 because the model fails to account for a dimer pathway that has the potential to
268 dominate the flux through oligomers. It has been suggested that oligomer
269 associations may be important during spontaneous microtubule assembly
270 (Erickson and Pantaloni, 1981; Mozziconacci et al., 2008; Voter and Erickson,
271 1984), but to our knowledge these interactions have not previously been
272 implemented into kinetic models.

Incorporating a dimer pathway fails to recapitulate experimental data without invoking a switch in lateral affinity

The cartoons and calculations presented in Fig. 2D,E illustrate how the rate of initiating a new lateral layer will depend on the concentration of longitudinal dimers of αβ-tubulin. By contrast, once the slow step of *initiating* a new layer has occurred, *zipping up* via addition into favorable 'corner' (longitudinal + lateral) sites should occur almost exclusively via αβ-tubulin 'monomers' because these monomers far exceed longitudinal dimers in number/concentration. By a similar logic, it is also not necessary to include a dimer pathway for initiating a longitudinal layer: lateral dimers are very rare, and the 'upper' αβ-tubulin of a longitudinal dimer provides no increased stabilization as a longitudinal layer builds up.

Incorporating a parallel, dimer-based pathway for initiating lateral layers (Sup. Fig. 4) requires that at each step we specify (i) the concentration of longitudinal dimers, (ii) an association rate constant for the longitudinal dimers adding to a complete layer, and (iii) a dissociation rate constant for the lateral 'unbinding' of a longitudinal dimer. The concentration of longitudinal dimers is easily calculated given the concentration of monomers and the equilibrium constant for longitudinal interactions. Because off-rate constants tend to vary over a much larger range than on-rate constants, for simplicity we used the same, roughly diffusion limited association rate constant as we do for monomers. We derived a formula that expresses the equilibrium constant for lateral association of a longitudinal dimer solely in terms of biochemical properties of the monomers (see Methods). Thus, we were able to parameterize the 'dimer pathway' purely in terms of the fundamental monomer properties.

We first fit the dimer model to individual assembly curves, as we did for the monomer model (Fig. 3A). The longitudinal and corner affinities for these dimer

303 model fits were comparable to those obtained from fits of the monomer model.
304 The lateral affinity (~25-30 M in the dimer model) was ~300-fold weaker than the
305 in the monomer model (~100 mM), reflecting a greatly diminished contribution of
306 the monomer pathway for lateral initiation. Although it was predicted to be
307 required biochemically, including this dimer pathway actually degraded the ability
308 of the model to recapitulate the shape of individual assembly curves compared to
309 the monomer-only fits: the simulated assembly curves displayed a less
310 pronounced lag phase and also appeared less cooperative (shallower sigmoid
311 transition; compare Fig. 3A to Fig. 2B). Global fits of the dimer model to the set of
312 assembly curves were also markedly poorer than for the monomer model (Fig.
313 3B). Thus, a more complete biochemical model for the assembly process
314 paradoxically degraded its predictive power.
315
316 Why was the monomer-only model able to fit the observed assembly curves so
317 much better than a model incorporating a dimer pathway? The presence of a
318 dimer pathway makes the effective rates of lateral and longitudinal growth much
319 more comparable to each other (Fig. 2D, compare top and bottom rate
320 expressions), whereas in the monomer-only model there is significantly more
321 contrast between the rates for longitudinal and lateral growth. We speculated that
322 the otherwise more accurate monomer+dimer model must still be missing a
323 critical feature that acts to increase the difference between longitudinal and
324 lateral growth.
325
326 What might be missing? Not having accounted for the effects of conformational
327 changes in αβ-tubulin that occur during microtubule formation (Ayaz et al., 2012;
328 Nawrotek et al., 2011; Pecqueur et al., 2012; Wang and Nogales, 2005) is a
329 strong candidate. Indeed, it is now well established that unpolymerized αβ-tubulin
330 subunits adopt a 'curved' conformation in solution and that the microtubule lattice
331 itself acts as an allosteric activator to 'straighten' αβ-tubulin during the assembly
332 process (Ayaz et al., 2012; Buey et al., 2006; Nawrotek et al., 2011; Rice et al.,

333 2008). That is, αβ-tubulin becomes progressively straighter as it becomes
334 increasingly surrounded by lateral neighbors (reviewed in (Brouhard and Rice,
335 2018)) (Fig. 4A). This straightening-induced conformational strain acts to weaken
336 lateral interactions in assemblies that require more straightening. To explore
337 these ideas in the context of our model, we introduced a very simple lateral
338 penalty to mimic the greater strain intrinsic to straighter conformations. We
339 assumed that two-wide assemblies could remain curved, whereas wider
340 assemblies would be forced to straighten, making the lateral interactions after the
341 first pairing in a given 'row' X-fold weaker.
342
343 We fit the monomer+dimer+penalty model to the data as before, testing a range
344 of penalty magnitudes (from 1 to 16 in Fig. 4B). The global fit to the experimental
345 curves improved as the magnitude of the lateral penalty increased, with the best
346 fits reached for penalty values greater than 4. Thus, penalizing lateral growth was
347 sufficient to 'correct' the deficiencies of the simple dimer pathway, resulting in
348 even better fits (Fig. 4B,C; penalty value = 8,) than for the monomer-only model
349 (see Fig. 3B,C). Beyond a value of 4, the improvement in global fit only weakly
350 depends on the precise value of the penalty (Fig. 4B). Fits to the alternative
351 dataset yielded similar but not identical affinities (Sup. Fig. 5). Other penalty
352 factors gave fits of comparable quality as long as the penalty factor was greater
353 than 4 (Fig. 4B), but yielded different longitudinal and lateral affinities, as
354 expected. Varying individual parameters shows that the fits are sensitive to small
355 (1.5-fold) changes in the parameter values (Sup. Fig. 6). Differences in the fitted
356 parameters for the primary and alternative dataset suggests that within a narrow
357 range there may be some compensation between corner and longitudinal
358 affinities (compare Fig. 4C to Sup. Fig. 5), Collectively, our computational
359 experiments led us to what we believe to be the first simple, biochemically-based
360 model that can accurately recapitulate the observed concentration-dependent
361 kinetics of spontaneous microtubule assembly without having to assume a
362 specific nucleus.

363

364 **A kinetically frustrated pathway for spontaneous microtubule assembly**

365 The model developed here provides a biochemical pathway that explains in a
366 new way why the kinetics of microtubule initiation are slow relative to polymer
367 elongation. As a first way to illustrate the assembly pathway that emerges from
368 fitting our model to the experimental data, we plotted the total concentration and
369 average size of intermediate oligomers as a function of time (Fig. 5A). The total
370 concentration of oligomers peaks at around 200 s in the example shown, and the
371 subsequent decrease is a consequence of the formation of microtubules and of
372 the depletion of free $\alpha\beta$-tubulin. The average oligomer size increases gradually
373 over several hundred seconds, reflecting the slow process of accretion and the
374 low likelihood that large layers will be lost in 'backward' reactions.

375

376 The endpoint of microtubule formation – closure of the cylindrical lattice –requires
377 a minimal width oligomer (13 in our model). Thus, we next examined the
378 summed concentration of tubulin oligomers with a given width (lateral extent) as
379 a function of time (Fig. 5B). This analysis shows that the concentration of
380 oligomers decreases as their width increases – there are fewer 3-wide oligomers
381 than 2-wide, fewer 4-wide then 3-wide, etc. (Fig. 5B). This decreasing
382 concentration of wider oligomers happens because the transition from one width
383 to the next accelerates throughout the assembly process. This acceleration can
384 be understood as a statistical/kinetic consequence of the two-dimensional
385 assembly pathway. No matter their height, all oligomers of a given width grow
386 *taller* with the same characteristic rate because they present the same number of
387 'landing sites' for starting a new longitudinal layer. However, taller oligomers
388 grow *wider* faster than shorter oligomers, because their increased height
389 provides more 'landing sites' for starting a new lateral layer. Similarly, wider
390 oligomers add longitudinal layers faster than the narrower ones for the same
391 reason.

392

To provide more granular insight into the nature of the predominant microtubule assembly intermediates, we examined the distribution of oligomer sizes at different widths (Fig. 5C). For each oligomer width, and at the time the concentration of oligomers of that width peaked, we plotted the most populated height (filled circle) and the relative amount of taller or shorter oligomers (grey teardrop/oval shapes, which are actually a set of circles with area scaled proportionally to the concentration). The many parallel pathways in the assembly process leads to an increasing spread in the range of oligomer heights as they get wider. For example, the most populated 50% of all 3-wide oligomers have heights between 7 and 11 (a height range of 5) whereas the most populated 50% of all 12-wide oligomers span heights between 50 and 64 (a height range of 15, three times greater than for 3-wides). The most populated immediate microtubule precursor (12 subunits wide) contains almost 700 tubulins: 58 subunits tall x 12 wide. This is much larger than the number of subunits in the nucleus predicted by phenomenological models (Flyvbjerg et al., 1996; Kuchnir Fygenson et al., 1995). Also note that the rate of layer assembly cannot exceed the rate of elongation. The layer-based assembly model thus provides a new, ensemble-based view of the assembly pathway wherein many oligomers of varying heights contribute appreciably to the formation of new microtubules.

Discussion

How existing microtubules grow and shrink is increasingly well-understood, but the understanding of how new microtubules form spontaneously – a related but mechanistically distinct process – lags behind (Roostalu and Surrey, 2017). Many discussions of spontaneous microtubule formation have invoked the concept of a ‘critical nucleus’, which is analogous to the transition-state of a chemical reaction (Kollman et al., 2011; Kuchnir Fygenson et al., 1995; Roostalu and Surrey, 2017; Voter and Erickson, 1984). This traditional view of the assembly pathway assumes that (i) the formation and growth of early

423 intermediates is thermodynamically unfavorable, and (ii) above a critical size,
424 oligomer growth by monomer addition becomes favorable and this elongation
425 proceeds at a fixed rate. The polymerization kinetics of relatively simple helical
426 polymers like actin can be well-described by two-step, nucleation-elongation
427 models that invoke a small critical nucleus representing a 'mini-filament' (the
428 smallest oligomeric species that presents helical binding sites) (Sept and
429 McCammon, 2001; Tobacman and Korn, 1983). However, the spontaneous
430 assembly kinetics of hollow, cylindrical microtubules do not conform to the
431 simplest two-step, nucleation-elongation kinetics (Flyvbjerg et al., 1996; Kuchnir
432 Fygenson et al., 1995; Voter and Erickson, 1984). Phenomenological multi-step
433 nucleation-elongation mechanisms (Flyvbjerg et al., 1996) can fit assembly
434 curves but fail to provide biochemical insights into the assembly pathway.
435
436 Our model provides an alternative and conceptually distinct framework for
437 thinking about the pathway for microtubule formation (Fig. 6), and the
438 biochemical factors that govern the overall rate of assembly. From this comes the
439 understanding that there is not a singular, transition-state-like species (variously
440 estimated as 8-27 tubulins) that dictates the assembly kinetics, but instead what
441 we would traditionally call "nucleation" arises from an ensemble of accretion
442 events involving many species and hundreds of tubulin heterodimers. In what
443 follows, we summarize the main features of the predicted assembly pathway and
444 discuss implications for the multiple ways that a template or other regulatory
445 factor could accelerate the process.
446
447 The layer growth model predicts that a multitude of pathways and intermediates
448 contribute meaningfully to microtubule assembly. Stronger longitudinal
449 interactions cause the dominant rectangular intermediates to be taller than they
450 are wide. Early in the assembly pathway, transitions to larger oligomers become
451 energetically favorable (equilibrium ratio less than one) but still occur slowly
452 because the oligomers are small and because initiating the new layer depends

453 on a weak individual longitudinal or lateral interaction. The rate of transition
454 between oligomers accelerates as oligomers increase in size, not because of any
455 intrinsic changes in the underlying affinities, but because larger oligomers
456 present more sites on which the next layer can initiate. These size-dependent
457 changes in transition rates are a direct consequence of the two-dimensional
458 nature of the assembly pathway. Thus, even though nearly all of the layer
459 additions are energetically 'downhill', the repeated difficulty of initiating each new
460 layer contributes a series of progressively smaller delays into the assembly
461 sequence that in combination represent the effective "barrier". Conformational
462 'straightening' of αβ-tubulins adds an additional kind of frustration that makes
463 lateral growth of early oligomers even harder. Collectively, the ensemble of
464 initiation barriers creates a kind of 'frustration' that dictates unique kinetics for
465 spontaneous microtubule assembly.
466
467 This layer-based view of the assembly pathway provides new ways for thinking
468 about how regulatory factors might accelerate microtubule initiation. Our
469 modeling indicates that the kinetics of microtubule formation are dictated by the
470 need for *repeated* 'layer' transitions that are limited by the weaker lateral affinity
471 and by the straightening penalty (e.g. Fig. 7A). Classical "nucleators" like the γ-
472 tubulin ring complex (γ-TuRC) (Zheng et al., 1995) contain a lateral array 14 γ-
473 tubulins (Fig. 7B) that are thought to form a 'template' on which a microtubule
474 can elongate (Consolati et al., 2020; Kollman et al., 2015; Kollman et al., 2011;
475 Liu et al., 2020; Moritz et al., 1995; Wieczorek et al., 2020). We used our model
476 to explore how the potency of templating might depend on the width of the
477 template. We modified our simulations to include various width templating
478 oligomers (Fig. 7C), using a constant total amount of templating 'monomers'.
479 Note that in these simulations there are progressively lower concentrations of the
480 wider oligomers (e.g. half as many 4-wide oligomers as 2-wide, etc.). The affinity
481 of αβ-tubulins for γ-TuRC is unknown, so we explored a regime where γ:αβ
482 longitudinal interactions are identical to αβ:αβ (Supplemental Fig. 7) and another

483 where γ:αβ longitudinal interactions are weaker than for αβ:αβ (Fig. 7). With the
484 stronger γ:αβ interaction strength, even 2-wide "templates" potently accelerated
485 assembly (Supplemental Fig. 7). This is at odds with experimental data showing
486 that γ-tubulin small complexes (γ-TuSCs), which only contain two γ-tubulins, are
487 much poorer nucleators than γ-TuRCs (Kollman et al., 2015; Oegema et al.,
488 1999). By contrast, when γ:αβ interactions were assumed to be weaker,
489 templating oligomers that were 2 subunits wide only modestly accelerated the
490 predicted assembly kinetics (1.1-fold faster characteristic time for assembly, $T_{0.1}$)
491 (Fig. 6C,D). A 3-wide oligomer was much more potent (1.7-fold faster) even
492 though in the simulations the concentration of 3-wide oligomers was less than
493 that of the 2-wide oligomer. This strong change in potency occurs because the
494 'hardest' transition in the assembly sequence is from two-wide oligomers to 3-
495 wide oligomers, providing an explanation for why γ-tubulin small complexes (γ-
496 TuSCs) only weakly stimulate assembly (Oegema et al., 1999). A recent study
497 provides experimental support for these prediction by showing that
498 γ:αβ interactions are weaker than αβ:αβ interactions (Thawani et al., 2020) In our
499 simulations, progressively wider templating arrays show even greater potency,
500 emphasizing that the barriers to lateral growth contribute throughout the entire
501 assembly pathway.
502
503 The idea that multiple reactions/transitions contribute to limit the overall rate of
504 microtubule formation also suggests that strategies besides templating could
505 enhance the rate of spontaneous assembly. The rates for layer additions depend
506 on how fast tubulins 'land' on the growing sheet, so enhancing this rate should
507 promote layer initiation and 'zippering'. For example, XMAP215 family
508 polymerases use an 'accelerated delivery' mechanism (Ayaz et al., 2014; Geyer
509 et al., 2018) to make microtubules grow faster, and this same activity likely
510 underlies the role for XMAP215 family proteins in microtubule nucleation
511 (Gunzelmann et al., 2018; Popov et al., 2002; Roostalu et al., 2015; Thawani et
512 al., 2018; Wieczorek et al., 2015). The efficiency of initiating new layers is

513 primarily limited by the relatively weak longitudinal or lateral affinities, especially
514 for the singleton tubulin that initiates each longitudinal layer. Thus, a factor that
515 stabilizes these associations should also increase the rate at which layer
516 transitions occur. Proteins like TPX2 and doublecortin bridge between
517 neighboring subunits in the lattice (Fourniol et al., 2010; Zhang et al., 2017); this
518 'molecular stapling' may help explain their documented roles in microtubule
519 "nucleation" (Moores et al., 2004; Roostalu et al., 2015). Finally, altering the
520 allosteric properties of αβ-tubulin itself should also profoundly affect microtubule
521 initiation. For example, and in keeping with predictions of our model, studies of
522 an αβ-tubulin 'conformation cycle' mutation (Geyer et al., 2015) that enhances
523 the strength of lateral interactions (Driver et al., 2017) (perhaps via reducing the
524 cost of αβ-tubulin straightening), greatly accelerates microtubule formation.
525 Similarly, small molecule compounds like taxol that stimulate microtubule
526 initiation and growth may do so by promoting straightening.
527
528 *Conclusions and perspective*
529 We described a relatively simple accretion model that explains spontaneous
530 microtubule assembly kinetics in terms of subunit biochemistry and an ensemble
531 of 'rectangular' intermediates. Whereas in typical 'nucleation-elongation'
532 paradigms the scarcity of the transition-state-like nucleus is what limits the rate of
533 polymer formation, our model is more akin to a process like crystal growth.
534 Indeed, in our accretion model most of the steps toward polymer formation are
535 energetically favorable but kinetically frustrated by the difficulty of initiating new
536 layers; this difficulty decreases as layers become larger because more landing
537 opportunities are presented. The accretion mechanism we describe is a direct
538 consequence of the two-dimensional nature of the hollow, cylindrical microtubule
539 lattice.
540
541 We did not consider the kinetic consequences of GTP hydrolysis within the
542 nascent polymer in our model, because it was not possible to account for the

stochastic hydrolysis within the context of our deterministic formalism. In keeping with that, our assay conditions were chosen to suppress microtubule catastrophe. We attempted to measure assembly curves in the presence of GMPCPP, a hydrolysis-resistant GTP analog, but obtained variable results because it was difficult to reliably eliminate contaminating amounts of microtubule seeds from the initial reaction mixtures. Ignoring GTPase activity represents a limitation of our model that we plan to address in future work. In general, GTPase activity should antagonize assembly by preferentially destabilizing intermediate oligomers, so the affinities we report may underestimate the 'true' affinities. We still expect that growth through accretion will represent the dominant pathway for assembly.

Finally, our model provides a unifying quantitative framework for understanding the complex effects of regulatory molecules. Indeed, the 'zippering' transitions between rectangular oligomers that dominate the initiation process also share many features in common with microtubule elongation. Thus, our model also explains why factors that regulate microtubule elongation and shrinking also regulate spontaneous microtubule assembly.

Acknowledgements
This study was supported by grants from the National Science Foundation to LMR (MCB-1615938 and MCB-1054947) and from the National Institutes of Health to DAA (R01 GM031627, R35 GM118099 and P01 GM105537). DAA was supported in part by the Howard Hughes Medical Institute. We thank T. Davis and her colleagues for very helpful feedback on the manuscript.

Author contributions
MM collected the microtubule assembly data and helped write the manuscript. LMR constructed models, fit the data, and drafted the manuscript. DAA analyzed data, supervised the research, and helped write the manuscript.

Methods

Measurements of spontaneous assembly

The spontaneous assembly of phosphocellulose-purified porcine-brain tubulin was followed by turbidity at 350 nm basically as described previously (Gaskin et al., 1974; Voter and Erickson, 1984). Care was taken to remove microtubule seeds and inactive protein by cycling it through an additional polymerization/depolymerization step just before use: immediately prior to performing assays, tubulin at –80°C was rapidly thawed at 37°, placed on an ice-water slurry (0°C), and the buffer was adjusted to 80 mM K-PIPES, pH 6.8, 1mM EGTA, 4 mM $MgCl_2$ and 1 mM GTP. After 5 min incubation, 0.5 volume of 37°C glycerol was mixed in and the tubulin was allowed to polymerize at 37°C for 20 min. Microtubules were pelleted through a 37°C, 60% glycerol cushion in 50 mM K-MES, pH 6.6, 5 mM $MgSO_4$, 1 mM EGTA, 1 mM GTP in a TLA110 rotor (Beckman, Palo Alto, CA) at 80,000 rpm, 20 min. The pellets were resuspended at 37°C in assembly buffer (AB: 50 mM K-MES, pH6.6, 3.4 M glycerol, 5 mM $MgSO_4$, 1 mM EGTA, 1 mM GTP) using a warm Potter homogenizer. The resuspended microtubules were then depolymerized on an ice-water slurry for 20 min and centrifuged in a TLA100.3 rotor at 100,000 rpm for 35 min at 2°C to remove any remaining polymerized tubulin. The supernatant from this cold spin was removed and used for the assembly reactions. The tubulin was kept at 0°C as reaction mixtures were prepared. A series of samples was prepared at different tubulin concentrations in AB and kept at 0°C in thin-walled, 0.5 ml plastic tubes (PCR tubes, Stratagene, Cedar Creek, TX). Samples were rapidly heated to 37°C directly in cuvettes pre-warmed to 37°C in a Pelltier cell changer (took 30 sec), in a custom built spectrophotometer. The $A_{350\ nm}$ was recorded approximately every 4 sec on 4 samples at a time until plateaus were reached. Recording on the spectrometer was started prior to transfer of tubulin to the cuvettes so that early lag-phase data were not missed. The time was adjusted to ignore the 30 sec heating step. Scaling analysis was performed using a customized program.

Explicit simulations in Berkeley Madonna

We constructed a model in Berkeley Madonna (Marcoline et al., 2020) to simulate αβ-tubulin self-assembly. The first step in this process was to define the set of αβ-tubulin oligomers and how they are related to each other by gain/loss of an αβ-tubulin though a longitudinal, lateral, or longitudinal+lateral ('corner') interaction. Starting from the two-dimensional nature of the microtubule lattice, we built a list of all possible configurations for an αβ-tubulin oligomer of a given size. Fig. 1 illustrates how there are two kinds of possible dimers of αβ-tubulin (longitudinal and lateral), three kinds of trimers of αβ-tubulin, etc. Larger oligomers can have multiple configurations that are energetically equivalent. To minimize the number of species and reactions considered in the model, we used a single exemplar species to represent each set of n-mers with the same number

of longitudinal and lateral contacts. For each exemplar species, population-weighted average rate constants were used to account for the different properties of each oligomer. Supplemental Figure 1 provides a worked example of this approximation for a tetramer of αβ-tubulin. We then used the 'Chemical Reactions' module in Berkeley Madonna (Marcoline et al., 2020) to build a set of rate equations corresponding to each possible transition. We did not pursue oligomers larger than 12-mers because the number of species and reactions became intractable. This model provides a way to analyze the rate and extent to which different species become populated for a given choice of the adjustable parameters.

Derivation of layer transition rates and validation in Berkeley Madonna

The explicit, monomer-based simulations in Berkeley Madonna (Marcoline et al., 2020) indicated that a simpler reaction scheme that only considered transitions between rectangular oligomers. We used the steady state approximation to derive effective rate constants for these transitions, as described below.

We will illustrate the derivation of layer-based transition rate constants using a specific example. Consider the layer-based reaction associated with adding a longitudinal layer onto an oligomer that is, say, n tubulins tall and 4 tubulins wide (in other words, the net reaction is (n,4) <--> (n+1,4). To simplify the notation, we will call the starting species **4** and the final species **4'**; the intermediates with one, two, and three tubulins on the layer will be called 4a, 4b, and 4c respectively. The individual reactions are:

$$4 + \alpha\beta \rightleftharpoons 4a \qquad (1)$$
$$4a + \alpha\beta \rightleftharpoons 4b \qquad (2)$$
$$4b + \alpha\beta \rightleftharpoons 4c \qquad (3)$$
$$4c + \alpha\beta \rightleftharpoons 4' \qquad (4)$$

The associated rate equations for these reactions, which account for the production and loss of intermediate species and also the fact that different configurations present different numbers of binding sites (Sup. Fig. 8), are:

$$\frac{d}{dt}[4a] = 8k_f[4][\alpha\beta] - k_r^{Long}[4a] - \frac{6}{4}k_f[4a][\alpha\beta] + 2k_r^{Corner}[4b] \qquad (5)$$
$$\frac{d}{dt}[4b] = \frac{6}{4}k_f[4a][\alpha\beta] - 2k_r^{Corner}[4b] - \frac{4}{3}k_f[4b][\alpha\beta] + 2k_r^{Corner}[4c] \qquad (6)$$
$$\frac{d}{dt}[4c] = \frac{4}{3}k_f[4b][\alpha\beta] - 2k_r^{Corner}[4c] - k_f[4c][\alpha\beta] \qquad (7)$$
$$\frac{d}{dt}[4'] = k_f[4c][\alpha\beta] \qquad (8)$$

Starting from the last intermediate 4c, we apply the steady-state approximation to the intermediate species to obtain an expression for the net rate of producing 4'

from 4. Assuming that the concentration of 4c does not change with time, its time derivative is zero, so:

$$\frac{d}{dt}[4c] = 0 \tag{9}$$

$$\Rightarrow \frac{4}{3}k_f[4b][\alpha\beta] - 2k_r^{Corner}[4c] - k_f[4c][\alpha\beta] = 0 \tag{10}$$

$$\Rightarrow \frac{4}{3}k_f[4b][\alpha\beta] = [4c]\left(k_f[\alpha\beta]+2k_r^{Corner}\right) \tag{11}$$

$$\Rightarrow [4c] = \frac{\frac{4}{3}k_f[\alpha\beta]}{\left(k_f[\alpha\beta]+2k_r^{Corner}\right)}[4b] \tag{12}$$

$$\Rightarrow [4c] = W_3[4b]\,, where\ W_3 = \frac{\frac{4}{3}k_f[\alpha\beta]}{\left(k_f[\alpha\beta]+2k_r^{Corner}\right)} \tag{13}$$

This yields an expression for the concentration of intermediate 4c in terms of its predecessor 4b. The multiplicative factor W_3 is given by the pseudo-first-order rate constant for forming 4c divided by the sum of the pseudo-first-order rate constants for losing 4c (in the forward or reverse direction).

This process can be applied again to obtain an expression for the concentration of intermediate 4b in terms of its predecessor 4a:

$$\frac{d}{dt}[4b] = 0 \tag{14}$$

$$\Rightarrow \frac{6}{4}k_f[4a][\alpha\beta] - 2k_r^{Corner}[4b] - \frac{4}{3}k_f[4b][\alpha\beta] + 2k_r^{Corner}[4c] = 0 \tag{15}$$

$$\Rightarrow \frac{6}{4}k_f[4a][\alpha\beta] - 2k_r^{Corner}[4b] - \frac{4}{3}k_f[4b][\alpha\beta] + 2k_r^{Corner}W_3[4b] = 0 \tag{16}$$

$$\Rightarrow [4b] = \frac{\frac{6}{4}k_f[\alpha\beta]}{\left(\frac{4}{3}k_f[\alpha\beta]+2k_r^{Corner} - 2k_r^{Corner}W_3\right)}[4a] \tag{17}$$

$$\Rightarrow [4b] = W_2[4a]\,, where\ W_2 = \frac{\frac{6}{4}k_f[\alpha\beta]}{\left(\frac{4}{3}k_f[\alpha\beta]+2k_r^{Corner} - 2k_r^{Corner}W_3\right)} \tag{18}$$

Where in (16) we eliminated [4c] by substituting W_3[4b], and in (17) we simply grouped terms in [4a] and [4b]. The weighting term W_2 is again given by a similar ratio as for W3, but with an additional term that includes W_3.

Applying the same procedure, we can obtain an expression for the concentration of the first intermediate 4a in terms of its predecessor, the rectangular species 4:

$$\frac{d}{dt}[4a] = 0 \tag{19}$$

$$\Rightarrow [4a] = \frac{8k_f[\alpha\beta]}{\left(\frac{6}{4}k_f[\alpha\beta]+k_r^{Long} - 2k_r^{Corner}W_2\right)}[4] \tag{20}$$

$$\Rightarrow [4a] = W_1[4], where\ W_1 = \frac{8k_f[\alpha\beta]}{\left(\frac{6}{4}k_f[\alpha\beta]+k_r^{Long} - 2k_r^{Corner}W_2\right)} \tag{21}$$

Finally, since the rate of finishing the layer is given by:

$$\frac{d}{dt}[4'] = k_f[4c][\alpha\beta] \tag{22}$$

$$\frac{d}{dt}[4'] = k_f W_3 W_2 W_1 [4][\alpha\beta] \tag{23}$$

Where in (23) we used (13) to eliminate [4c] for a term involving [4b], (18) to eliminate [4b] for a term involving [4a], and (21) to eliminate [4a] for a term involving [4]. This yields an apparent rate constant for adding a layer, the terms of which only involve the fundamental rate constants and multiplicative factors that account for the number of ways a particular reaction can happen. In the case presented there are three such terms because the layer contains 4 tubulins. Because k_r^{Corner} is small compared to $k_f[\alpha\beta]$, is can be neglected in the denominator and so all weights excepting the first one will be numbers between 1 and 2. W_1 contains k_r^{Long} in the denomimator, which in general is large compared to $k_f[\alpha\beta]$, so W_1 tends to be a small number that reflects the difficulty of initiating a new layer. The general procedure is formulaic and can be applied to any size layer.

The effective equilibrium ratio for the layer addition is given by

$$\begin{aligned} Layer\ equilibrium\ ratio &= \frac{[4]}{[4']} \\ &= \frac{K_d^{Long}(K_d^{Corner})^3}{[\alpha\beta]^4} \end{aligned}$$

Finally, we compute an effective rate constant for layer loss by multiplying the layer equilibrium ratio and the forward layer rate constant:

$$k_r^{Layer} = \left(k_f^{Layer}\right)(Layer\ \ equilibrium\ ratio) \tag{25}$$

$$k_r^{Layer} = \left(k_f W_3 W_2 W_1 [\alpha\beta]\right)\left(\frac{K_d^{Long}(K_d^{Corner})^3}{[\alpha\beta]^4}\right) \tag{26}$$

$$k_r^{Layer} = \left(k_f W_3 W_2 W_1\right)\left(\frac{K_d^{Long}\left(K_d^{Corner}\right)^3}{[\alpha\beta]^3}\right) \tag{27}$$

The preceding derivation was performed for the specific case of adding a longitudinal layer that is four subunits wide. For layers of size N, a similar logic applies with the following differences: (i) the kinetic weighting factors for the first through the $(N-1)^{th}$ subunit additions change to reflect the different number of configurations (Sup. Fig. 8), and (ii) there is a different number of multiplicative factors (*W_is*).

735 To determine if this reduced representation could accurately recapitulate the
736 timecourses for rectangular species in the explicit model, we constructed a new
737 model in Berkeley Madonna (Marcoline et al., 2020) (also truncated at 12-mers)
738 that considered monomer-based reactions to form the first rectangular
739 intermediate, a 2x2 tetramer of αβ-tubulin, but that only considered layer
740 transitions for larger species, using the layer rate laws described above. We input
741 expressions for the layer transition rates as derived above, and ran the
742 simulations using the same biochemical parameters used in the explicit
743 simulations. The layer model faithfully reproduced the results from the explicit
744 simulations (Fig. 1).
745
746 ***Layer-based simulations of microtubule self-assembly***
747 To enable simulations of arbitrarily large oligomers, we wrote a custom computer
748 program that effectively performs the same calculations of Berkeley Madonna but
749 in a more automated way that makes it easier to incorporate a much larger
750 number of species and reactions. The program automates the generation of the
751 list of possible rectangular oligomers [(2,2), (3,2), (2,3), etc.] and the recursive
752 calculation of rate constants for transitions between them (as explained above
753 and in Sup. Fig. 8). The program then integrates the set of transition rate laws
754 using finite-difference methods. At each time point, the program uses longitudinal
755 and lateral affinities along with the concentration of 'free' tubulin (here free
756 means the population not incorporated into rectangular oligomers (2,2) or larger)
757 to calculate the concentration of free tubulin 'monomers' and of longitudinal and
758 lateral dimers, and trimers assuming these species are all in rapid equilibrium
759 (see box in Fig. 1E); using these quantities, the program then takes a small step
760 forward in time, updating quantities of all rectangular oligomers according to the
761 rate laws and the layer rate constants. This results in an updated set of
762 concentrations for the rectangular oligomers (and hence of free tubulin), and the
763 process is repeated. To account for microtubule formation, we simply converted
764 species that became 13-protofilaments wide into microtubules, and we assumed
765 that microtubules elongated by monomer addition into a 'corner' site. We did not
766 explicitly consider the seam or the variable configuration of the microtubule end,
767 and for simplicity we assumed plus- and minus-ends elongated with identical
768 kinetics. We used a downhill simplex algorithm to fit the simulated timecourses to
769 the experimental ones, using fraction of tubulin in rectangular oligomers as a
770 proxy for the normalized assembly data.
771
772 ***Derivation of the equilibrium constant for lateral association of a pre-***
773 ***formed longitudinal dimer***
774 To implement the dimer pathway (Fig. 2 and Sup. Fig. 4), we assume that the on-
775 rate constant for adding a dimer is the same as for adding a monomer. Given the
776 on-rate constant, we obtain the off-rate constant (for the initiating dimer to
777 dissociate) using the equilibrium constant for the dimer binding. We show here
778 that this new equilibrium constant can be calculated purely in terms of 'monomer'

properties. First, we write the dissociation constants in terms of free energies of association, as follows:

$$K_d^{Long} = e^{\Delta G^{Long} + \Delta S}$$

$$K_d^{Lat} = e^{\Delta G^{Lat} + \Delta S}$$

$$K_d^{Corner} = e^{\Delta G^{Long} + \Delta G^{Lat} + \Delta S}$$

where we have separated out the entropic cost of subunit immobilization (loss of rotational and translational degrees of freedom) as ΔS as has been done previously (e.g. (Erickson and Pantaloni, 1981; VanBuren et al., 2002)). The reason for doing this separation is that lateral association of a pre-formed longitudinal dimer should have the same entropic 'cost' as for association of a monomer (because the cost of losing rotational and translational degrees of freedom is already built in to the longitudinal affinity). The K_d values are the fitted parameters in the model.

What we wish to calculate is the dissociation constant for two simultaneous lateral contacts:

$$K_d^{2-Lat} = e^{2\Delta G^{lat} - \Delta S}$$

We prove here that:

$$K_d^{2-lat} = K_d^{Lat} * \left(K_d^{Corner} \Big/ K_d^{Long} \right)$$

$$\begin{aligned} K_d^{Lat} * \left(K_d^{Corner} \Big/ K_d^{Long} \right) &= e^{\Delta G^{Lat} + \Delta S} * \left(e^{\Delta G^{Long} + \Delta G^{Lat} + \Delta S} \Big/ e^{\Delta G^{Long} + \Delta S} \right) \\ &= e^{\Delta G^{Lat} + \Delta S} * \left(e^{\Delta G^{Long} + \Delta G^{Lat} + \Delta S - \Delta G^{Long} - \Delta S} \right) \\ &= e^{\Delta G^{Lat} + \Delta S} * \left(e^{\Delta G^{Lat}} \right) \\ &= e^{2 * \Delta G^{Lat} + \Delta S} \end{aligned}$$

Simulating the effects of template-like nucleators

To investigate the effects of template-like nucleators in the model, we modified the simulations to include an additional template species. We assumed a constant total concentration of 'monomers' that were distributed into templating oligomers of different widths. This assumption means that progressively wider oligomers are present in the simulations at progressively lower concentrations; for example, for a given concentration of templating monomers, there will be half as many 4-wide oligomers as 2-wide, and so on. For calculating the rate constants for the first layer addition onto the template, we assumed that only one longitudinal interface of this templating oligomer (the plus end) was active for nucleation.

In initial runs wherein interactions between γ- and αβ-tubulin were assumed to be of identical affinity, we observed potent nucleation even from templates that were only two subunits wide (Supplemental Fig. 7). Because two-wide nucleators like

the γ-TuSC are much less potent than 12-14-wide oligomers like the γ-TuRC (Kollman et al., 2015; Oegema et al., 1999), we also performed simulations with 10-fold weaker interactions between γ- and αβ-tubulin than for αβ:αβ interactions (Fig. 6)

826 **References**
827

828 Akhmanova, A., and M.O. Steinmetz. 2015. Control of microtubule organization and
829 dynamics: two ends in the limelight. *Nat Rev Mol Cell Biol*. 16:711-726.
830 Alushin, G.M., G.C. Lander, E.H. Kellogg, R. Zhang, D. Baker, and E. Nogales. 2014.
831 High-resolution microtubule structures reveal the structural transitions in
832 alphabeta-tubulin upon GTP hydrolysis. *Cell*. 157:1117-1129.
833 Ayaz, P., S. Munyoki, E.A. Geyer, F.A. Piedra, E.S. Vu, R. Bromberg, Z. Otwinowski, N.V.
834 Grishin, C.A. Brautigam, and L.M. Rice. 2014. A tethered delivery mechanism
835 explains the catalytic action of a microtubule polymerase. *Elife*. 3:e03069.
836 Ayaz, P., X. Ye, P. Huddleston, C.A. Brautigam, and L.M. Rice. 2012. A TOG:alphabeta-
837 tubulin complex structure reveals conformation-based mechanisms for a
838 microtubule polymerase. *Science*. 337:857-860.
839 Barlan, K., and V.I. Gelfand. 2017. Microtubule-Based Transport and the Distribution,
840 Tethering, and Organization of Organelles. *Cold Spring Harb Perspect Biol*. 9.
841 Brouhard, G.J., and L.M. Rice. 2018. Microtubule dynamics: an interplay of
842 biochemistry and mechanics. *Nat Rev Mol Cell Biol*. 19:451-463.
843 Buey, R.M., J.F. Diaz, and J.M. Andreu. 2006. The nucleotide switch of tubulin and
844 microtubule assembly: a polymerization-driven structural change.
845 *Biochemistry*. 45:5933-5938.
846 Burton, P.R., R.E. Hinkley, and G.B. Pierson. 1975. Tannic acid-stained microtubules
847 with 12, 13, and 15 protofilaments. *J Cell Biol*. 65:227-233.
848 Chaaban, S., S. Jariwala, C.T. Hsu, S. Redemann, J.M. Kollman, T. Muller-Reichert, D.
849 Sept, K.H. Bui, and G.J. Brouhard. 2018. The Structure and Dynamics of C.
850 elegans Tubulin Reveals the Mechanistic Basis of Microtubule Growth. *Dev*
851 *Cell*. 47:191-204 e198.
852 Chalfie, M., and J.N. Thomson. 1982. Structural and functional diversity in the
853 neuronal microtubules of Caenorhabditis elegans. *J Cell Biol*. 93:15-23.
854 Consolati, T., J. Locke, J. Roostalu, Z.A. Chen, J. Gannon, J. Asthana, W.M. Lim, F.
855 Martino, M.A. Cvetkovic, J. Rappsilber, A. Costa, and T. Surrey. 2020.
856 Microtubule Nucleation Properties of Single Human gammaTuRCs Explained
857 by Their Cryo-EM Structure. *Dev Cell*. 53:603-617 e608.
858 Coombes, C.E., A. Yamamoto, M.R. Kenzie, D.J. Odde, and M.K. Gardner. 2013.
859 Evolving tip structures can explain age-dependent microtubule catastrophe.
860 *Curr Biol*. 23:1342-1348.
861 Davis, C., and K. Gull. 1983. Protofilament number in microtubules in cells of two
862 parasitic nematodes. *J Parasitol*. 69:1094-1099.
863 Desai, A., and T.J. Mitchison. 1997. Microtubule polymerization dynamics. *Annu Rev*
864 *Cell Dev Biol*. 13:83-117.
865 Driver, J.W., E.A. Geyer, M.E. Bailey, L.M. Rice, and C.L. Asbury. 2017. Direct
866 measurement of conformational strain energy in protofilaments curling
867 outward from disassembling microtubule tips. *Elife*. 6.
868 Duellberg, C., N.I. Cade, D. Holmes, and T. Surrey. 2016. The size of the EB cap
869 determines instantaneous microtubule stability. *Elife*. 5.

870 Erickson, H.P., and D. Pantaloni. 1981. The role of subunit entropy in cooperative
871 assembly. Nucleation of microtubules and other two-dimensional polymers.
872 *Biophys J*. 34:293-309.
873 Flyvbjerg, H., E. Jobs, and S. Leibler. 1996. Kinetics of self-assembling microtubules:
874 an "inverse problem" in biochemistry. *Proc Natl Acad Sci U S A*. 93:5975-
875 5979.
876 Fourniol, F.J., C.V. Sindelar, B. Amigues, D.K. Clare, G. Thomas, M. Perderiset, F.
877 Francis, A. Houdusse, and C.A. Moores. 2010. Template-free 13-protofilament
878 microtubule-MAP assembly visualized at 8 A resolution. *J Cell Biol*. 191:463-
879 470.
880 Gardner, M.K., B.D. Charlebois, I.M. Janosi, J. Howard, A.J. Hunt, and D.J. Odde. 2011.
881 Rapid microtubule self-assembly kinetics. *Cell*. 146:582-592.
882 Gaskin, F., C.R. Cantor, and M.L. Shelanski. 1974. Turbidimetric studies of the in vitro
883 assembly and disassembly of porcine neurotubules. *J Mol Biol*. 89:737-755.
884 Geyer, E.A., A. Burns, B.A. Lalonde, X. Ye, F.A. Piedra, T.C. Huffaker, and L.M. Rice.
885 2015. A mutation uncouples the tubulin conformational and GTPase cycles,
886 revealing allosteric control of microtubule dynamics. *Elife*. 4:e10113.
887 Geyer, E.A., M.P. Miller, C.A. Brautigam, S. Biggins, and L.M. Rice. 2018. Design
888 principles of a microtubule polymerase. *Elife*. 7.
889 Grishchuk, E.L., M.I. Molodtsov, F.I. Ataullakhanov, and J.R. McIntosh. 2005. Force
890 production by disassembling microtubules. *Nature*. 438:384-388.
891 Gunzelmann, J., D. Ruthnick, T.C. Lin, W. Zhang, A. Neuner, U. Jakle, and E. Schiebel.
892 2018. The microtubule polymerase Stu2 promotes oligomerization of the
893 gamma-TuSC for cytoplasmic microtubule nucleation. *Elife*. 7.
894 Holy, T.E., and S. Leibler. 1994. Dynamic instability of microtubules as an efficient
895 way to search in space. *Proc Natl Acad Sci U S A*. 91:5682-5685.
896 Kim, T., and L.M. Rice. 2019. Long-range, through-lattice coupling improves
897 predictions of microtubule catastrophe. *Mol Biol Cell*. 30:1451-1462.
898 Kollman, J.M., C.H. Greenberg, S. Li, M. Moritz, A. Zelter, K.K. Fong, J.J. Fernandez, A.
899 Sali, J. Kilmartin, T.N. Davis, and D.A. Agard. 2015. Ring closure activates
900 yeast gammaTuRC for species-specific microtubule nucleation. *Nat Struct Mol*
901 *Biol*. 22:132-137.
902 Kollman, J.M., A. Merdes, L. Mourey, and D.A. Agard. 2011. Microtubule nucleation by
903 gamma-tubulin complexes. *Nat Rev Mol Cell Biol*. 12:709-721.
904 Kuchnir Fygenson, D., H. Flyvbjerg, K. Sneppen, A. Libchaber, and S. Leibler. 1995.
905 Spontaneous nucleation of microtubules. *Phys Rev E Stat Phys Plasmas Fluids*
906 *Relat Interdiscip Topics*. 51:5058-5063.
907 Kwiatkowska, M., K. Poplonska, D. Stepinski, and Z. Hejnowicz. 2006. Microtubules
908 with different diameter, protofilament number and protofilament spacing in
909 Ornithogalum umbellatum ovary epidermis cells. *Folia Histochem Cytobiol*.
910 44:133-138.
911 Liu, P., E. Zupa, A. Neuner, A. Bohler, J. Loerke, D. Flemming, T. Ruppert, T. Rudack, C.
912 Peter, C. Spahn, O.J. Gruss, S. Pfeffer, and E. Schiebel. 2020. Insights into the
913 assembly and activation of the microtubule nucleator gamma-TuRC. *Nature*.
914 578:467-471.

915 Manka, S.W., and C.A. Moores. 2018. The role of tubulin-tubulin lattice contacts in
916 the mechanism of microtubule dynamic instability. *Nat Struct Mol Biol*.
917 25:607-615.
918 Marcoline, F., M. Grabe, S. Nayak, T. Zahnley, G. Oster, and R. Macey. 2020. Berkeley
919 Madonna User's Guide.
920 Margolin, G., I.V. Gregoretti, T.M. Cickovski, C. Li, W. Shi, M.S. Alber, and H.V.
921 Goodson. 2012. The mechanisms of microtubule catastrophe and rescue:
922 implications from analysis of a dimer-scale computational model. *Mol Biol*
923 *Cell*. 23:642-656.
924 McIntosh, J.R., E. O'Toole, G. Morgan, J. Austin, E. Ulyanov, F. Ataullakhanov, and N.
925 Gudimchuk. 2018. Microtubules grow by the addition of bent guanosine
926 triphosphate tubulin to the tips of curved protofilaments. *J Cell Biol*.
927 217:2691-2708.
928 Mitchison, T., and M. Kirschner. 1984. Dynamic instability of microtubule growth.
929 *Nature*. 312:237-242.
930 Moores, C.A., M. Perderiset, F. Francis, J. Chelly, A. Houdusse, and R.A. Milligan. 2004.
931 Mechanism of microtubule stabilization by doublecortin. *Mol Cell*. 14:833-
932 839.
933 Moritz, M., M.B. Braunfeld, J.W. Sedat, B. Alberts, and D.A. Agard. 1995. Microtubule
934 nucleation by gamma-tubulin-containing rings in the centrosome. *Nature*.
935 378:638-640.
936 Mozziconacci, J., L. Sandblad, M. Wachsmuth, D. Brunner, and E. Karsenti. 2008.
937 Tubulin dimers oligomerize before their incorporation into microtubules.
938 *PLoS One*. 3:e3821.
939 Nawrotek, A., M. Knossow, and B. Gigant. 2011. The determinants that govern
940 microtubule assembly from the atomic structure of GTP-tubulin. *J Mol Biol*.
941 412:35-42.
942 Oegema, K., C. Wiese, O.C. Martin, R.A. Milligan, A. Iwamatsu, T.J. Mitchison, and Y.
943 Zheng. 1999. Characterization of two related Drosophila gamma-tubulin
944 complexes that differ in their ability to nucleate microtubules. *J Cell Biol*.
945 144:721-733.
946 Pecqueur, L., C. Duellberg, B. Dreier, Q. Jiang, C. Wang, A. Pluckthun, T. Surrey, B.
947 Gigant, and M. Knossow. 2012. A designed ankyrin repeat protein selected to
948 bind to tubulin caps the microtubule plus end. *Proc Natl Acad Sci U S A*.
949 109:12011-12016.
950 Piedra, F.A., T. Kim, E.S. Garza, E.A. Geyer, A. Burns, X. Ye, and L.M. Rice. 2016. GDP-
951 to-GTP exchange on the microtubule end can contribute to the frequency of
952 catastrophe. *Mol Biol Cell*. 27:3515-3525.
953 Popov, A.V., F. Severin, and E. Karsenti. 2002. XMAP215 is required for the
954 microtubule-nucleating activity of centrosomes. *Curr Biol*. 12:1326-1330.
955 Prosser, S.L., and L. Pelletier. 2017. Mitotic spindle assembly in animal cells: a fine
956 balancing act. *Nat Rev Mol Cell Biol*. 18:187-201.
957 Rice, L.M., E.A. Montabana, and D.A. Agard. 2008. The lattice as allosteric effector:
958 structural studies of alphabeta- and gamma-tubulin clarify the role of GTP in
959 microtubule assembly. *Proc Natl Acad Sci U S A*. 105:5378-5383.

960 Roostalu, J., N.I. Cade, and T. Surrey. 2015. Complementary activities of TPX2 and
961 chTOG constitute an efficient importin-regulated microtubule nucleation
962 module. *Nat Cell Biol*. 17:1422-1434.
963 Roostalu, J., and T. Surrey. 2017. Microtubule nucleation: beyond the template. *Nat*
964 *Rev Mol Cell Biol*. 18:702-710.
965 Saito, K., and K. Hama. 1982. Structural diversity of microtubules in the supporting
966 cells of the sensory epithelium of guinea pig organ of Corti. *J Electron Microsc*
967 *(Tokyo)*. 31:278-281.
968 Sept, D., and J.A. McCammon. 2001. Thermodynamics and kinetics of actin filament
969 nucleation. *Biophys J*. 81:667-674.
970 Thawani, A., R.S. Kadzik, and S. Petry. 2018. XMAP215 is a microtubule nucleation
971 factor that functions synergistically with the gamma-tubulin ring complex.
972 *Nat Cell Biol*. 20:575-585.
973 Thawani, A., M.J. Rale, N. Coudray, G. Bhabha, H.A. Stone, J.W. Shaevitz, and S. Petry.
974 2020. The transition state and regulation of gamma-TuRC-mediated
975 microtubule nucleation revealed by single molecule microscopy. *Elife*. 9.
976 Tobacman, L.S., and E.D. Korn. 1983. The kinetics of actin nucleation and
977 polymerization. *J Biol Chem*. 258:3207-3214.
978 Tucker, J.B., C.C. Paton, G.P. Richardson, M.M. Mogensen, and I.J. Russell. 1992. A cell
979 surface-associated centrosomal layer of microtubule-organizing material in
980 the inner pillar cell of the mouse cochlea. *J Cell Sci*. 102 (Pt 2):215-226.
981 VanBuren, V., L. Cassimeris, and D.J. Odde. 2005. Mechanochemical model of
982 microtubule structure and self-assembly kinetics. *Biophys J*. 89:2911-2926.
983 VanBuren, V., D.J. Odde, and L. Cassimeris. 2002. Estimates of lateral and
984 longitudinal bond energies within the microtubule lattice. *Proc Natl Acad Sci*
985 *U S A*. 99:6035-6040.
986 Voter, W.A., and H.P. Erickson. 1984. The kinetics of microtubule assembly. Evidence
987 for a two-stage nucleation mechanism. *J Biol Chem*. 259:10430-10438.
988 Wang, H.W., and E. Nogales. 2005. Nucleotide-dependent bending flexibility of
989 tubulin regulates microtubule assembly. *Nature*. 435:911-915.
990 Wieczorek, M., S. Bechstedt, S. Chaaban, and G.J. Brouhard. 2015. Microtubule-
991 associated proteins control the kinetics of microtubule nucleation. *Nat Cell*
992 *Biol*. 17:907-916.
993 Wieczorek, M., L. Urnavicius, S.C. Ti, K.R. Molloy, B.T. Chait, and T.M. Kapoor. 2020.
994 Asymmetric Molecular Architecture of the Human gamma-Tubulin Ring
995 Complex. *Cell*. 180:165-175 e116.
996 Zakharov, P., N. Gudimchuk, V. Voevodin, A. Tikhonravov, F.I. Ataullakhanov, and E.L.
997 Grishchuk. 2015. Molecular and Mechanical Causes of Microtubule
998 Catastrophe and Aging. *Biophys J*. 109:2574-2591.
999 Zhang, R., G.M. Alushin, A. Brown, and E. Nogales. 2015. Mechanistic Origin of
1000 Microtubule Dynamic Instability and Its Modulation by EB Proteins. *Cell*.
1001 162:849-859.
1002 Zhang, R., J. Roostalu, T. Surrey, and E. Nogales. 2017. Structural insight into TPX2-
1003 stimulated microtubule assembly. *Elife*. 6.
1004 Zheng, Y., M.L. Wong, B. Alberts, and T. Mitchison. 1995. Nucleation of microtubule
1005 assembly by a gamma-tubulin-containing ring complex. *Nature*. 378:578-583.

Figure 1

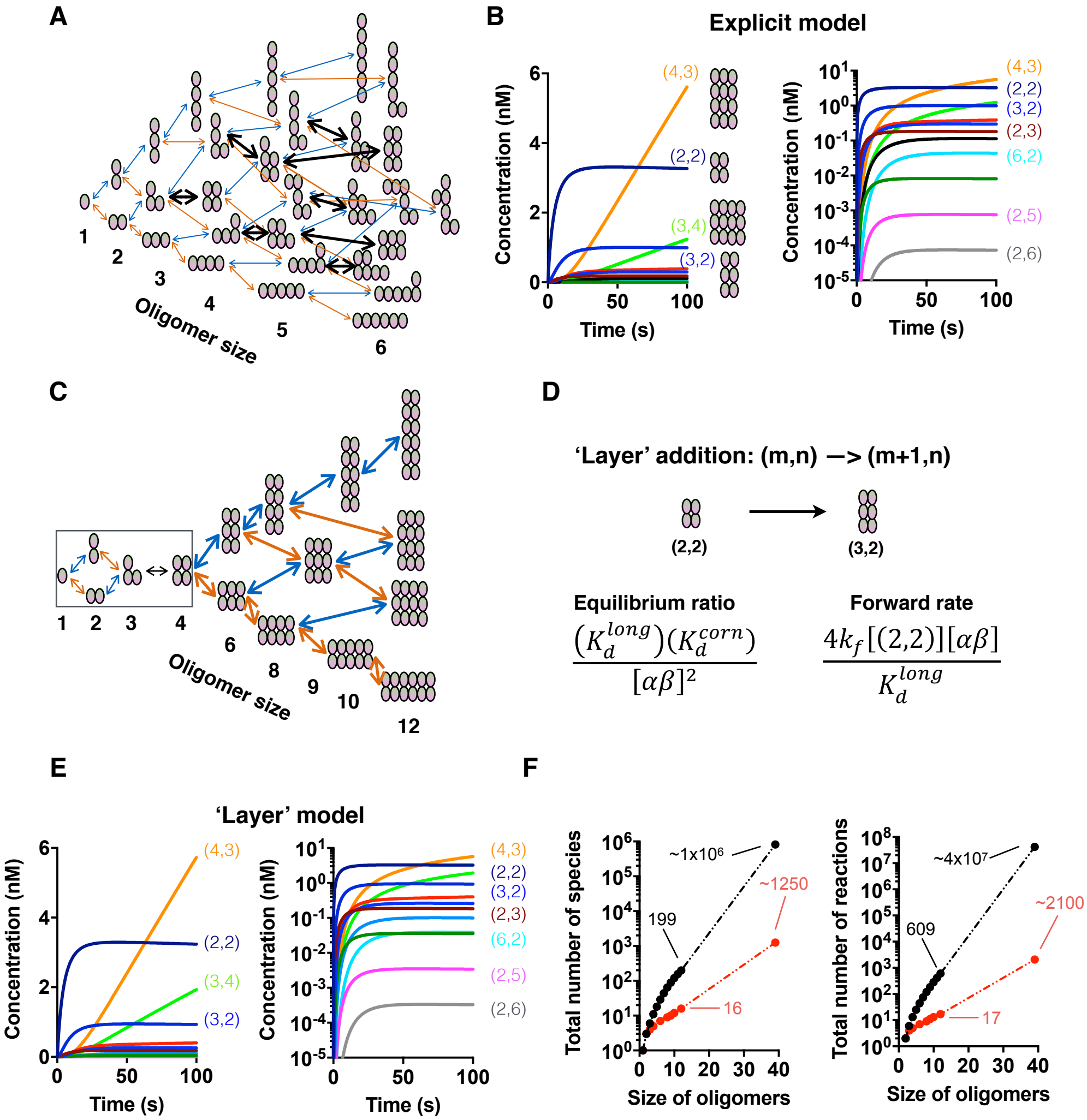
A
1
2
3
4
5
6
Oligomer size
B
Explicit model
Concentration (nM)
Time (s)
(4,3)
(2,2)
(3,4)
(3,2)
(2,3)
(6,2)
(2,5)
(2,6)
C
1 2 3 4
6
8
9
10
12
Oligomer size
D
'Layer' addition: (m,n) —> (m+1,n)
(2,2)
(3,2)
Equilibrium ratio
$\frac{(K_d^{long})(K_d^{corn})}{[\alpha\beta]^2}$
Forward rate
$\frac{4k_f[(2,2)][\alpha\beta]}{K_d^{long}}$
E
'Layer' model
F
Total number of species
Total number of reactions
Size of oligomers
~1x10⁶
~1250
199
16
~4x10⁷
~2100
609
17

Figure 1 An explicit biochemical model for early steps in spontaneous microtubule nucleation.

A Cartoon of the model. Individual αβ-tubulin heterodimers (ovals) can associate longitudinally (blue arrows) or laterally (orange arrows). As oligomers grow in size, they can present sites where an associating tubulin would simultaneously make longitudinal and lateral interactions ("corner"; bold black arrows). The resulting collection of species and reactions was implemented in BerkeleyMadonna (Macey et al., 2009) for simulations. Species up to 6-mers are shown, but the model includes species up to 12-mers. Rapid growth of the number of oligomers and reactions with size made it impractical to consider even larger oligomers.

B (left) Plot showing that 'rectangular' species dominate the simulation. The four dominant species are shown, with values in parentheses indicating the height and width for the oligomers. (right) The same data plotted on a logarithmic concentration scale. Other rectangular oligomers are much less common. Non-rectangular oligomers are not shown, but are also much rarer than the dominant oligomers shown.

C A simplified 'layer growth' model that only considers rectangular oligomers. Arrows indicate longitudinal (blue) or lateral (orange) layer growth. The resulting collection of species and reactions was implemented in BerkeleyMadonna for simulations (see Methods)

D Cartoon of a 'layer' addition reaction with associated rate constants. The equilibrium ratio and rate for layer addition can be defined in terms of underlying longitudinal, lateral, and corner affinities and a single on rate constant. An effective equilibrium constant and an approximation of the effective forward rate constant for this layer addition are shown. See Methods for derivations.

E Similar to **B** but showing results from simulations of the simplified layer model. This much simpler model with many fewer species and reactions quantitatively reproduces results from the explicit model.

F (left) Plot of the species count for all possible oligomers (black) and for the subset of rectangular oligomers (red). The extrapolation to a 40-mer emphasizes the magnitude of the simplification. (right) Similar plot but for the number of biochemical reactions.

Figure 2

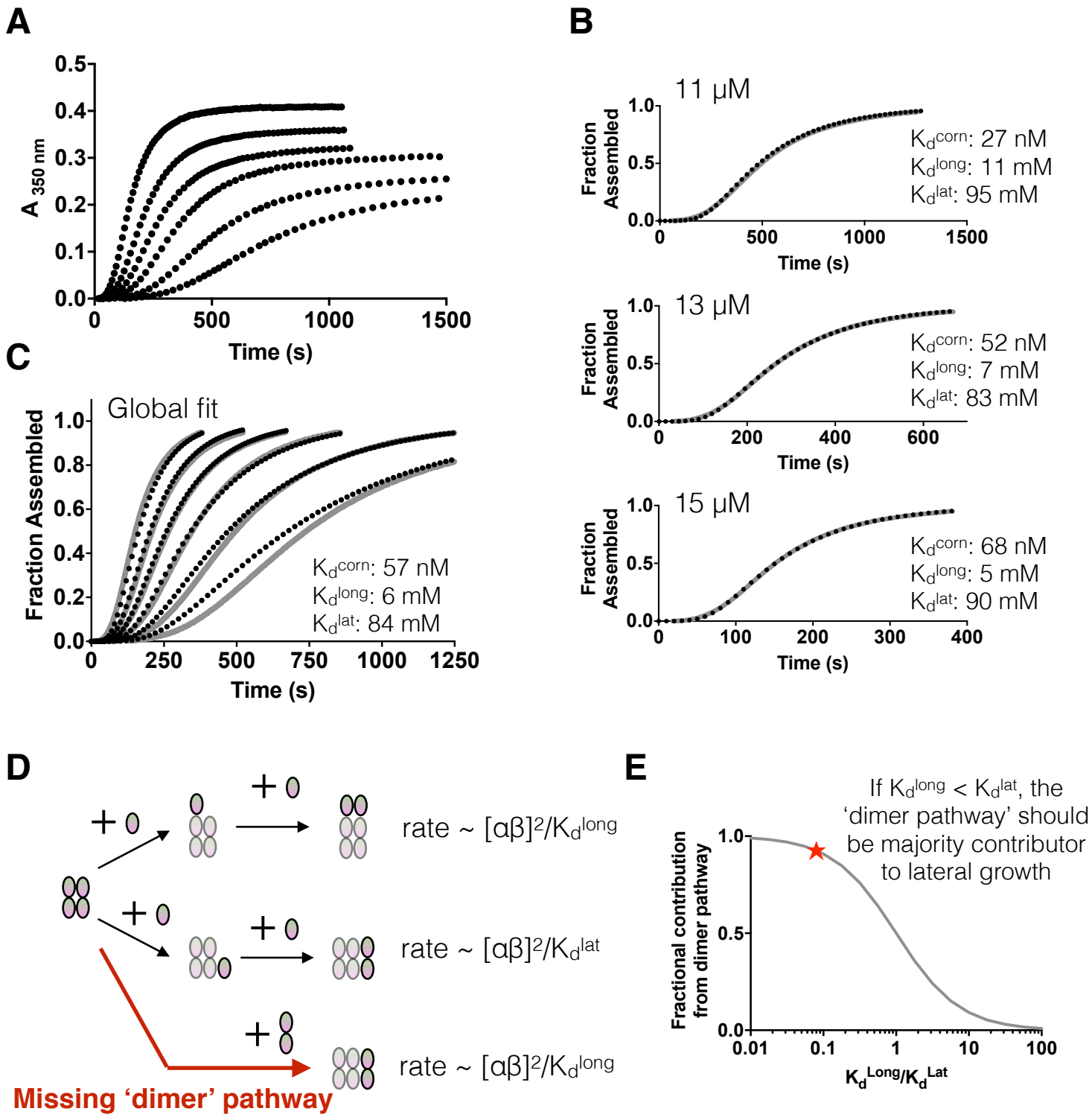
A
A 350 nm
Time (s)
B
11 μM
13 μM
15 μM
Fraction Assembled
Time (s)
Kd corn: 27 nM
Kd long: 11 mM
Kd lat: 95 mM
Kd corn: 52 nM
Kd long: 7 mM
Kd lat: 83 mM
Kd corn: 68 nM
Kd long: 5 mM
Kd lat: 90 mM
C
Global fit
Fraction Assembled
Time (s)
Kd corn: 57 nM
Kd long: 6 mM
Kd lat: 84 mM
D
rate ~ [αβ]2/Kd long
rate ~ [αβ]2/Kd lat
rate ~ [αβ]2/Kd long
Missing 'dimer' pathway
E
If Kd long < Kd lat, the 'dimer pathway' should be majority contributor to lateral growth
Fractional contribution from dimer pathway
Kd Long/Kd Lat

1040 **Figure 2** Expansion of the layer model to arbitrarily large oligomers for simulating
1041 spontaneous microtubule nucleation. Oligomers are allowed to become arbitrarily
1042 tall. We assumed that when oligomers reached a width of 13, they 'closed' into a
1043 tube and elongated by monomer addition.
1044 **A** Spontaneous microtubule nucleation kinetics measured by turbidity ($A_{350\ nm}$) at
1045 multiple concentrations of αβ-tubulin (10, 11, 12, 13, 14, 15 μM).
1046 **B** Fits of the model (black dotted line) to individual assembly curves (solid grey
1047 line) at the indicated concentration. Fits to individual curves are good. Inset text
1048 shows the resulting longitudinal, lateral, and 'corner' (simultaneous longitudinal
1049 and lateral interactions) affinities, which differ somewhat from run to run.
1050 **C** Global fit of the model (black dashed lines) to the full set of assembly data
1051 (grey lines). As evidenced by the poor fit at low concentration, the model
1052 underestimates the concentration-dependence of the progress curves.
1053 **D** Cartoon illustrating that longitudinal dimers of αβ-tubulin should contribute to
1054 lateral growth. The associated forward rates for the indicated reactions are
1055 shown.
1056 **E** The relative contribution of 'monomer' and 'dimer' initiation pathways can be
1057 estimated as indicated based on the affinities of longitudinal and lateral
1058 interactions. Plot predicting the fractional contribution of a 'dimer' pathway for
1059 lateral growth in terms of the relative strength of longitudinal and lateral
1060 interactions. The red star indicates the ratio obtained from the fit shown in **B**.
1061 Those parameters predict that the 'dimer' pathway should dominate the
1062 assembly, but it is not accounted for in our model.
1063

Figure 3

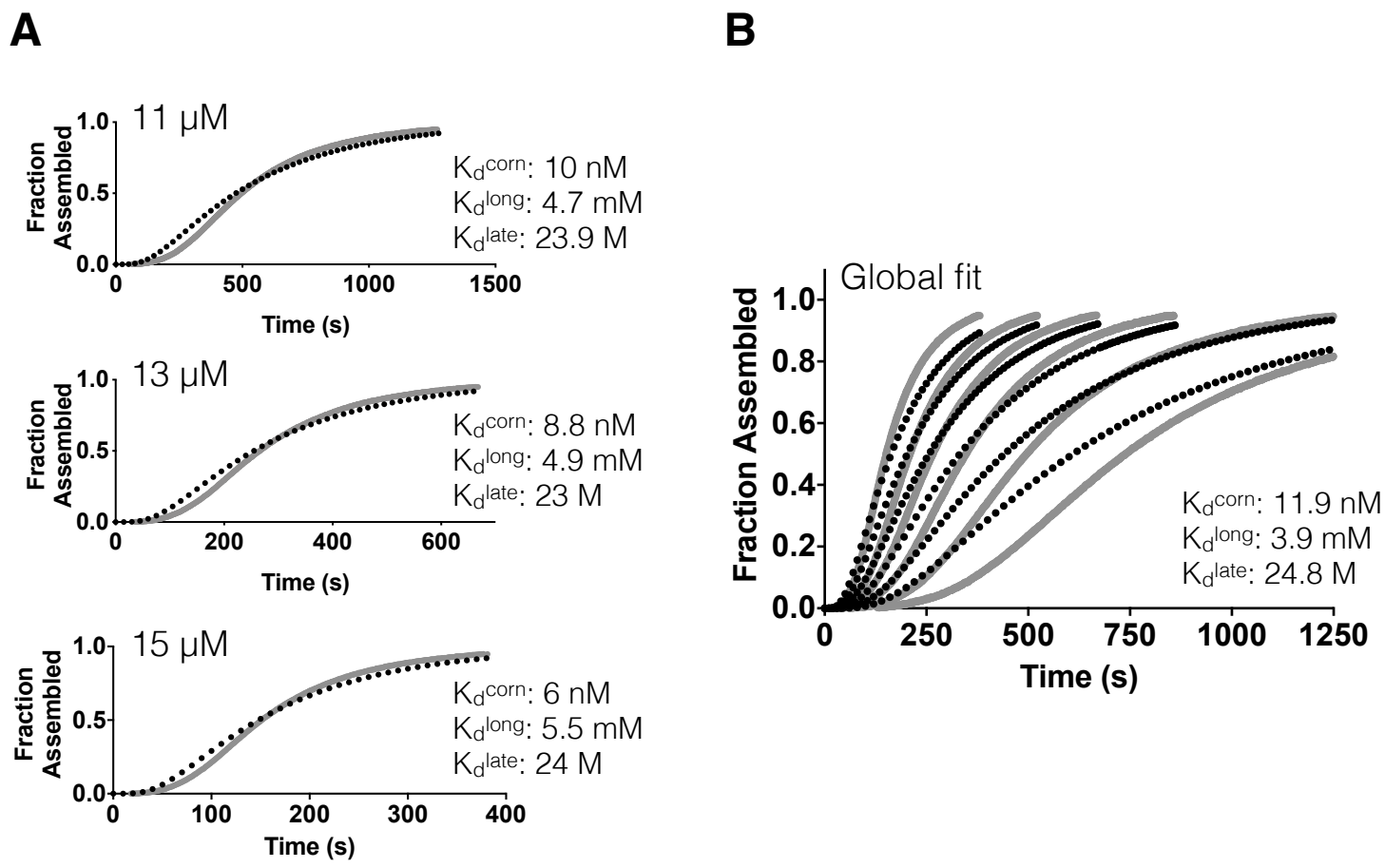
A
11 μM
Fraction Assembled
1.0
0.5
0.0
0
500
1000
1500
Time (s)
K_d^{corn}: 10 nM
K_d^{long}: 4.7 mM
K_d^{late}: 23.9 M
13 μM
Fraction Assembled
1.0
0.5
0.0
0
200
400
600
Time (s)
K_d^{corn}: 8.8 nM
K_d^{long}: 4.9 mM
K_d^{late}: 23 M
15 μM
Fraction Assembled
1.0
0.5
0.0
0
100
200
300
400
Time (s)
K_d^{corn}: 6 nM
K_d^{long}: 5.5 mM
K_d^{late}: 24 M
B
Global fit
Fraction Assembled
1.0
0.8
0.6
0.4
0.2
0.0
0
250
500
750
1000
1250
Time (s)
K_d^{corn}: 11.9 nM
K_d^{long}: 3.9 mM
K_d^{late}: 24.8 M

Figure 3 Incorporating a dimer pathway for lateral growth into the model
A Fits of the new dimer model (black dotted line) to individual assembly curves (solid grey line) at the indicated concentrations. Fits to individual curves are worse than for the monomer only model (compare to Fig. 2B). Inset text shows the resulting longitudinal, lateral, and 'corner' (simultaneous longitudinal and lateral interactions) affinities; the corner affinity varies almost two-fold over for 11 and 15 μM fits. The lateral affinity is ~200-fold weaker than for 'monomer model' fits, reflecting the dominance of the dimer pathway in this model.
B Global fit of the model (black dashed lines) to the full set of assembly data (grey lines). The fit is poor, with the model predicting too fast assembly at all concentrations.

Figure 4

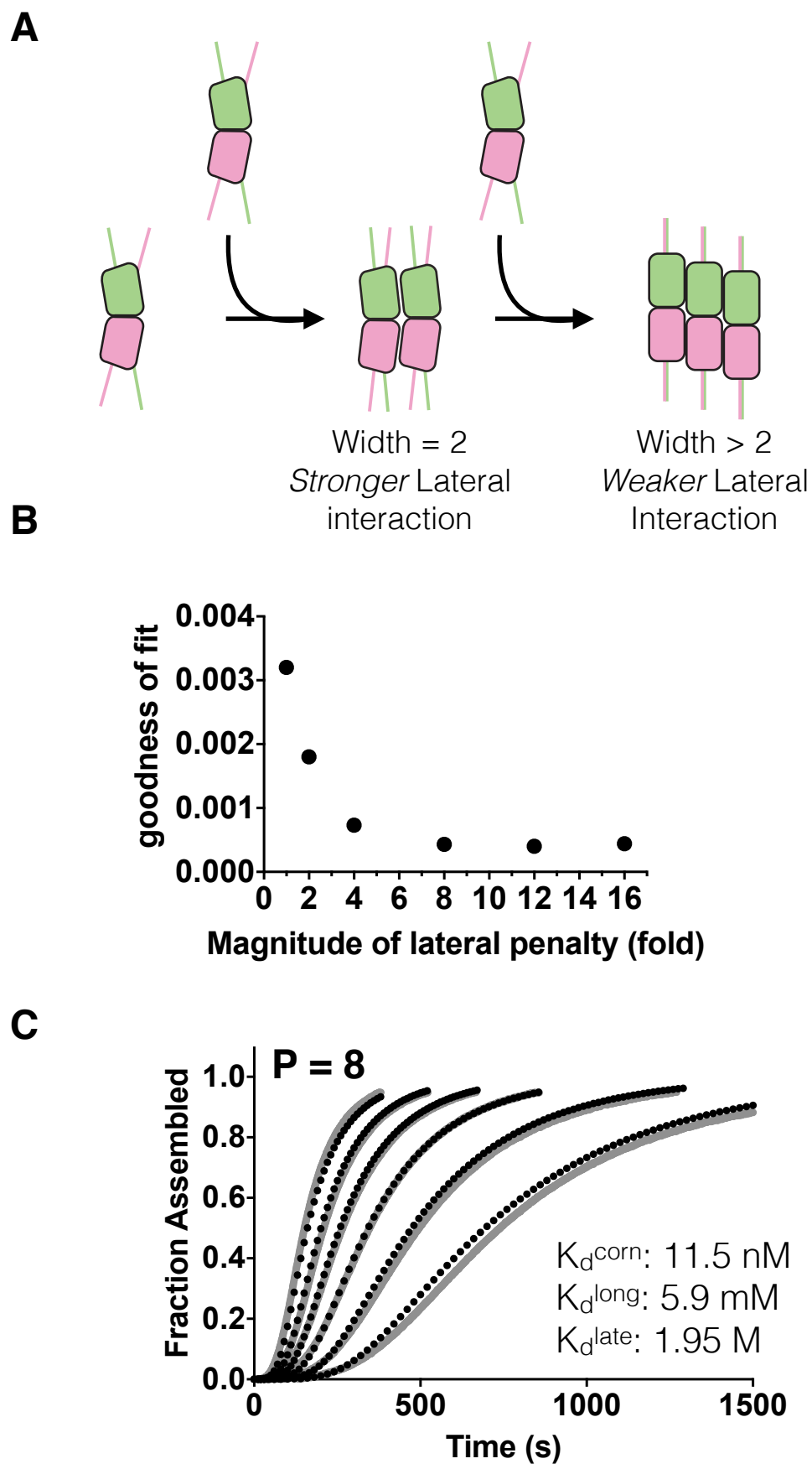
A
Width = 2
Stronger Lateral interaction
Width > 2
Weaker Lateral Interaction
B
goodness of fit
0.004
0.003
0.002
0.001
0.000
0 2 4 6 8 10 12 14 16
Magnitude of lateral penalty (fold)
C
P = 8
Fraction Assembled
1.0
0.8
0.6
0.4
0.2
0.0
0 500 1000 1500
Time (s)
K_d^{corn}: 11.5 nM
K_d^{long}: 5.9 mM
K_d^{late}: 1.95 M

Figure 4 A 'penalty' that mimics the cost of αβ-tubulin straightening markedly improves the performance of the dimer model

A Cartoons illustrating αβ-tubulin straightening, which is thought to occur progressively with width (the number of lateral neighbors). To model this in a very simple way, we introduced a penalty to make lateral interactions weaker for the 3rd and successive lateral interactions.

B Performance of the 'dimer with penalty' model as a function of penalty strength. The improved goodness of fit from the global optimization is not very sensitive to the magnitude of the penalty, as long as the penalty is ~8 or greater.

C Illustration of the model fit to the experimental data for a penalty value of 8. Inset shows fitted affinities (the corner affinity given here is for width=2 interactions, i.e. before application of the penalty).

Figure 5

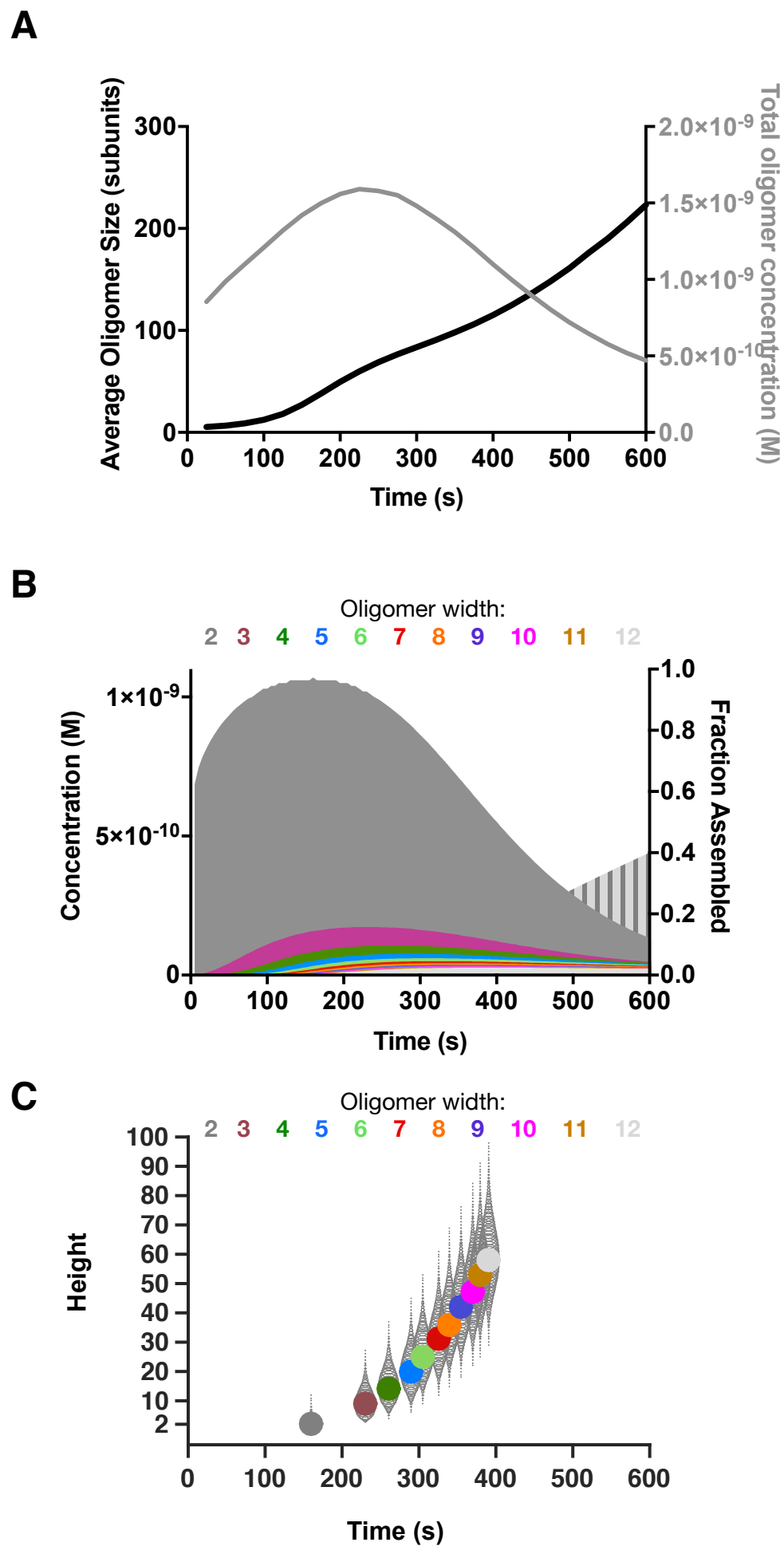
A
Average Oligomer Size (subunits)
Total oligomer concentration (M)
Time (s)
B
Oligomer width:
2 3 4 5 6 7 8 9 10 11 12
Concentration (M)
Fraction Assembled
Time (s)
C
Oligomer width:
2 3 4 5 6 7 8 9 10 11 12
Height
Time (s)

Figure 5 Different ways of representing the predicted pathway for spontaneous microtubule assembly

A The average size of intermediate oligomers (black curve) increases slowly over time. The total concentration of intermediate oligomers increases and then decreases, an effect that can be explained by depletion of free αβ-tubulin, and the formation of microtubules.

B Summed concentration for all oligomers of a given width, plotted as a function of time. Oligomers with width=2 dominate. Wider oligomers become progressively rarer and peak at increasingly late times, reflecting the obstacles to lateral growth. The vertically striped light grey curve behind the others shows the extent of total assembly (right y-axis).

C Distribution of oligomer heights as a function of their width. The most populated height is plotted as a filled circle for each width (different colors), at the time that width peaks. Other height oligomers at a given width are plotted as open circles, with the radius reflecting their concentration relative to the peak species. The time to transition from one width to the next decreases as oligomers get wider and taller, and the spread of oligomer heights increases as oligomers get wider.

Figure 6

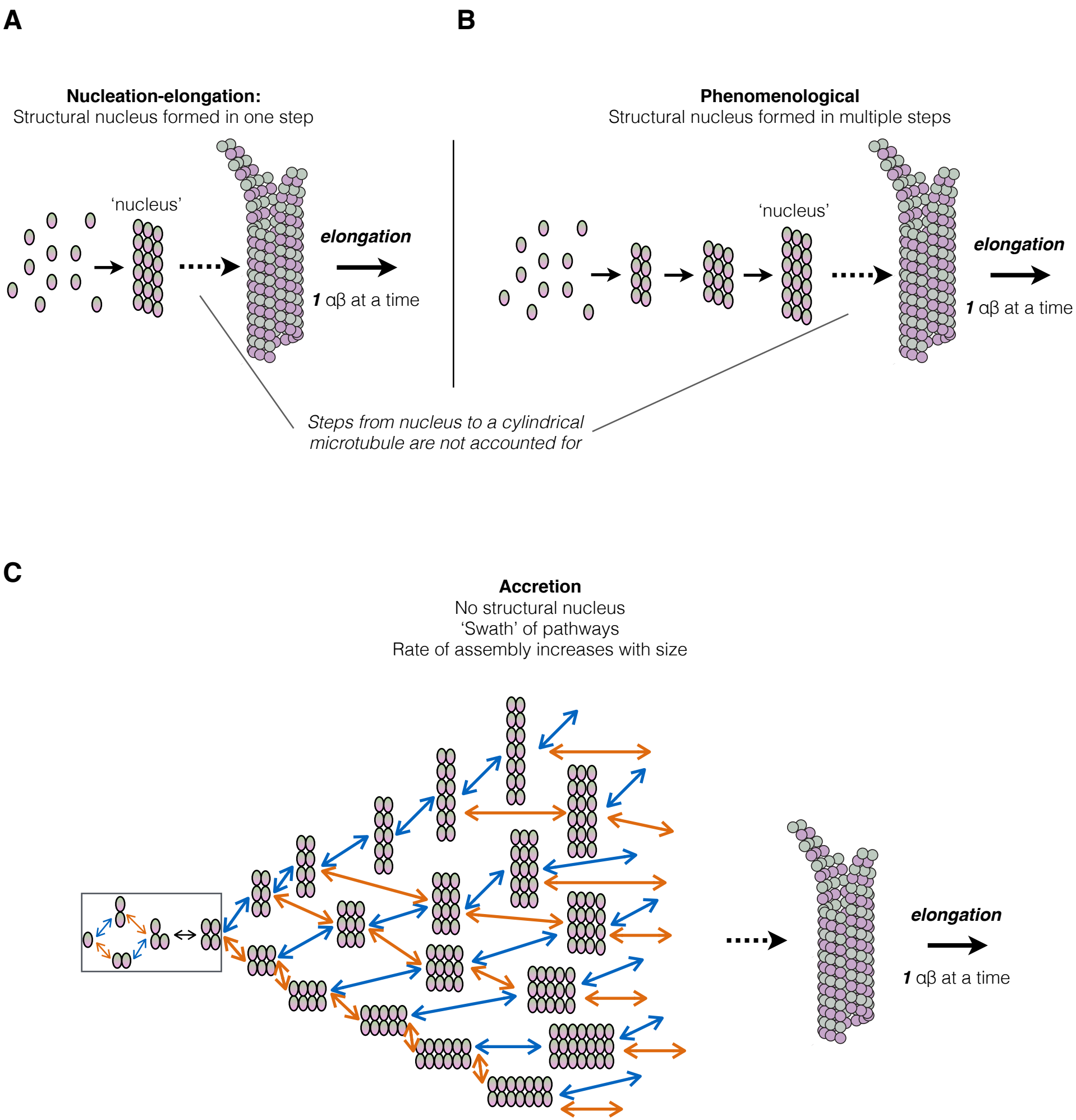
A
Nucleation-elongation:
Structural nucleus formed in one step
'nucleus'
elongation
1 αβ at a time
B
Phenomenological
Structural nucleus formed in multiple steps
'nucleus'
elongation
1 αβ at a time
Steps from nucleus to a cylindrical microtubule are not accounted for
C
Accretion
No structural nucleus
'Swath' of pathways
Rate of assembly increases with size
elongation
1 αβ at a time

Figure 6 Summary of accretion model and comparison with nucleation-elongation models

A Cartoon illustrating a classic nucleation-elongation model in which the rate of polymer formation is limited by the concentration of a rare species (the nucleus) that is in a rapid equilibrium with unpolymerized subunits (ovals). Such models cannot account for the additional steps/species in between the nucleus and the formation of the cylindrical microtubule.

B Cartoon illustrating a phenomenological model (Flyvbjerg et al., 1996) that differs from nucleation-elongation model in that the nucleus is formed in multiple steps. In this model the rate of polymer formation is also limited by the concentration of a rare species (the nucleus), and there is no accounting for the additional steps/species in between the nucleus and the formation of the cylindrical microtubule.

C Cartoon illustrating the accretion model presented in this paper. In this model there are many pathways to form a cylindrical microtubule, and all 'layer accretion' steps are described. In this accretion model, and in contrast with nucleation-elongation and phenomenological models, most of the steps toward polymer formation are energetically favorable but kinetically frustrated by the difficulty of initiating new layers. These barriers to initiation decrease as oligomers become larger, as in crystal growth, and it is the ensemble of pathways and barriers that define the kinetics of microtubule formation.

Figure 7

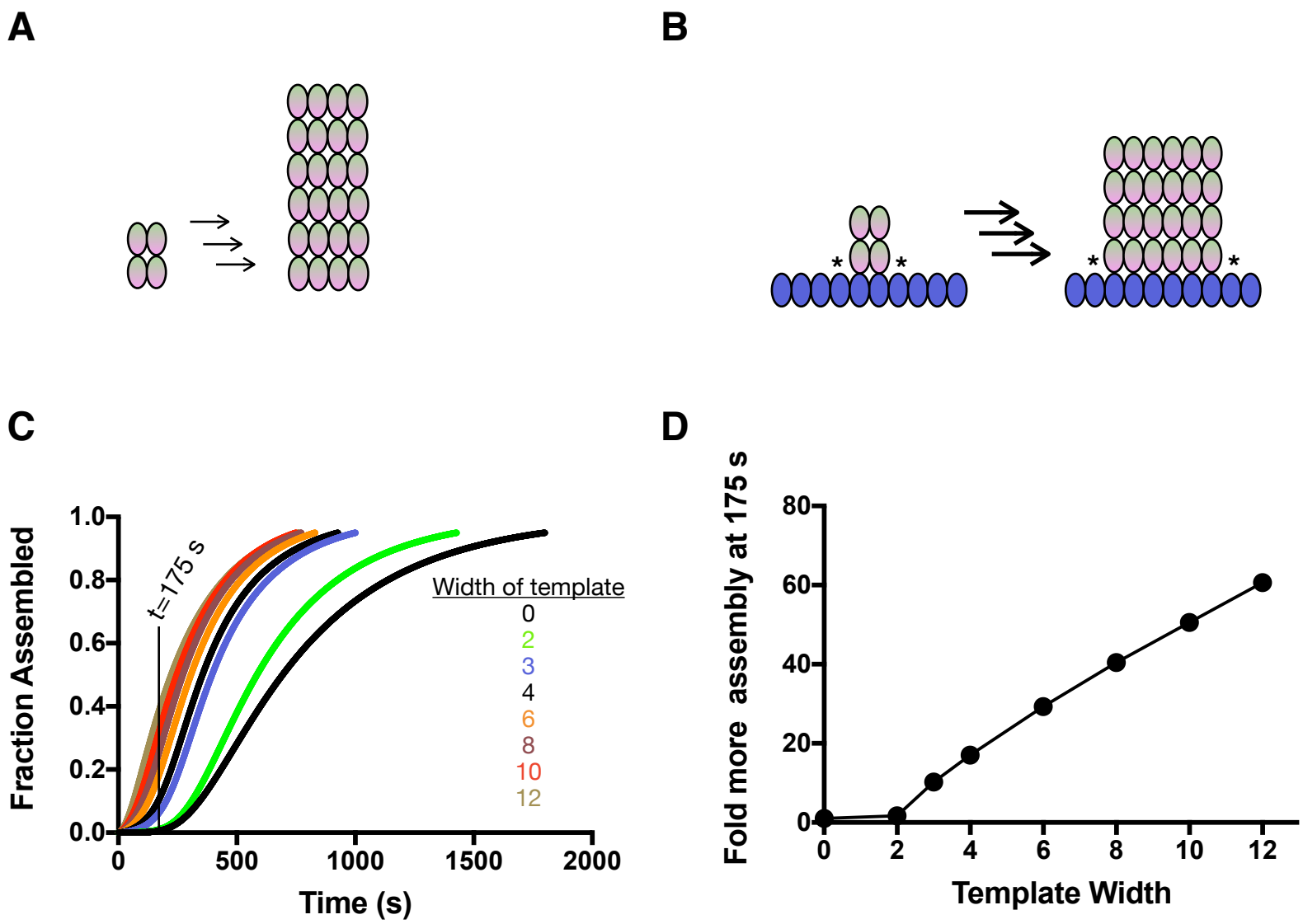
A
B
C
D
Fraction Assembled
1.0
0.8
0.6
0.4
0.2
0.0
0
500
1000
1500
2000
Time (s)
t=175 s
Width of template
0
2
3
4
6
8
10
12
Fold more assembly at 175 s
80
60
40
20
0
0
2
4
6
8
10
12
Template Width

Figure 7 Implications for templating microtubule assembly

A Cartoon illustrating an intermediate stage of spontaneous nucleation. 2x2 oligomers of αβ-tubulin (left) assemble as described into rectangular intermediates that tend to be taller than they are wide (middle) because of the barriers to lateral growth. Arrows indicate multiple layer additions, each one associated with a delay.

B When αβ-tubulin adds to a γ-TuRC-like template, cartooned here as a row of blue ovals, the barrier to lateral growth is eliminated because 'corner' sites form at the border of the αβ-tubulin oligomer. This accelerates the accretion process (bolder arrows indicating faster transitions) and the resulting oligomers now tend to be wider than they are tall

C Simulated nucleation curves in the presence of γ-tubulin templates of different width assuming γ:αβ interactions are weaker than αβ:αβ interactions. The total concentration of templating monomers is held constant. Templates that are only two subunits wide (bright green) show a modest effect, but wider templates are increasingly potent. The vertical line indicates the 175 s timepoint that we used for analysis in the next panel.

D Quantification of the data from C. Wider templates are more potent than narrower ones. Templating the earliest step in nucleation (from 2-wide to 3-wide) yields the most dramatic decrease in $T_{0.1}$.

E Fraction of αβ-tubulin incorporated into microtubules at an early time (here, 175 s, see vertical line in panel C) plotted as a function of template width and using data from C. Relative assembly at a given time represents the fraction assembled for a given template divided by the fraction assembled in the untemplated control. The changes in nucleation kinetics can result in large changes in the overall degree of microtubule assembly at early times.

Illustration of the meaning of 'non-redundant' oligomers

There are 6 distinct αβ-tubulin tetramers with 2 longitudinal bonds and 1 lateral bond

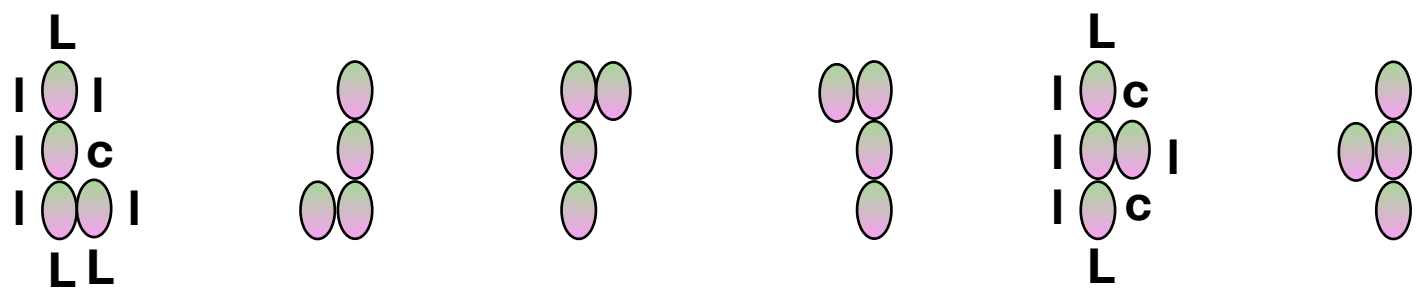

These 4 species present :
1 corner (c),
3 longitudinal (L), and
5 lateral (l) binding sites

These 2 species present :
2 corner (c),
2 longitudinal (L), and
4 lateral (l) binding sites

All 6 oligomers can be modeled using a single species that presents the appropriate, population-weighted number of different binding site types:

Population-weighted average:
1.33 corner (c),
2.67 longitudinal (L), and
4.67 lateral (l) binding sites

Supplemental Figure 1 Illustration of the concept and implementation of 'non-redundant' oligomers. Representative configurations of an $\alpha\beta$-tubulin tetramer containing two longitudinal and one lateral bond are indicated. These are indistinguishable from the standpoint of binding energy, but differ in terms of the number and type of binding sites they present. Our algorithm simplifies these six species into one and uses population weighted rate constants to capture the 'average' number and type of binding sites presented.

Supplemental Figure 2

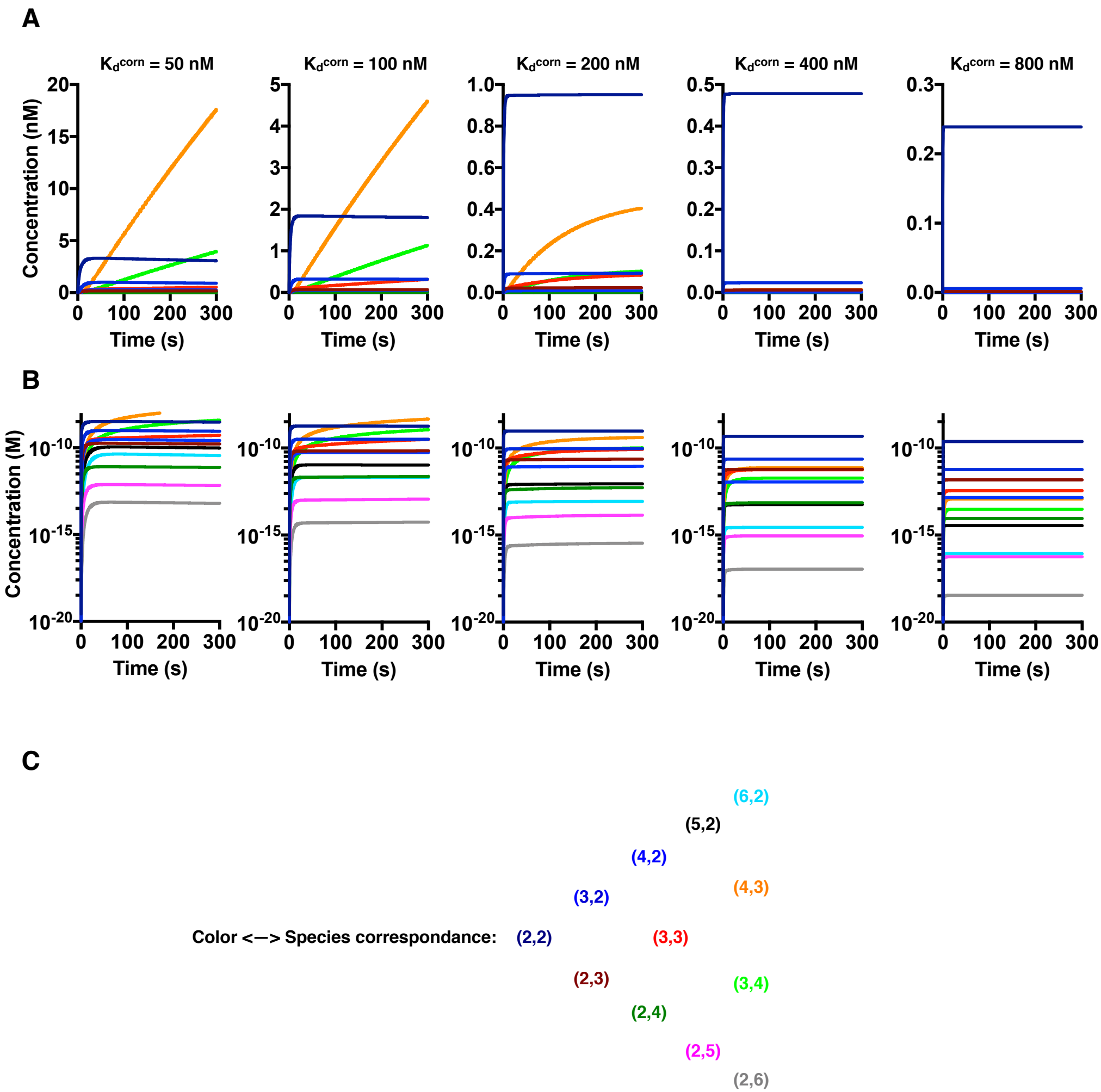

Supplemental Figure 2 In the explicit model, relatively tight corner affinity is required for appreciable assembly into larger oligomers.

A Plots of the concentration of 'rectangular' oligomers vs time, for different values of the corner affinity (color coding is given in panel C and is identical to that used in Fig. 2B). Note different y-axis ranges for different plots. At corner affinity of 400 nM and weaker, assembly into species larger than a tetramer of $\alpha\beta$-tubulin (dark blue curve) is negligeable.

B As in A, but using a log-scale y-axis to show the dramatic fall-off in the concentration of larger species.

C Legend showing the correspondence between color and oligomer dimensions.

Supplemental Figure 3

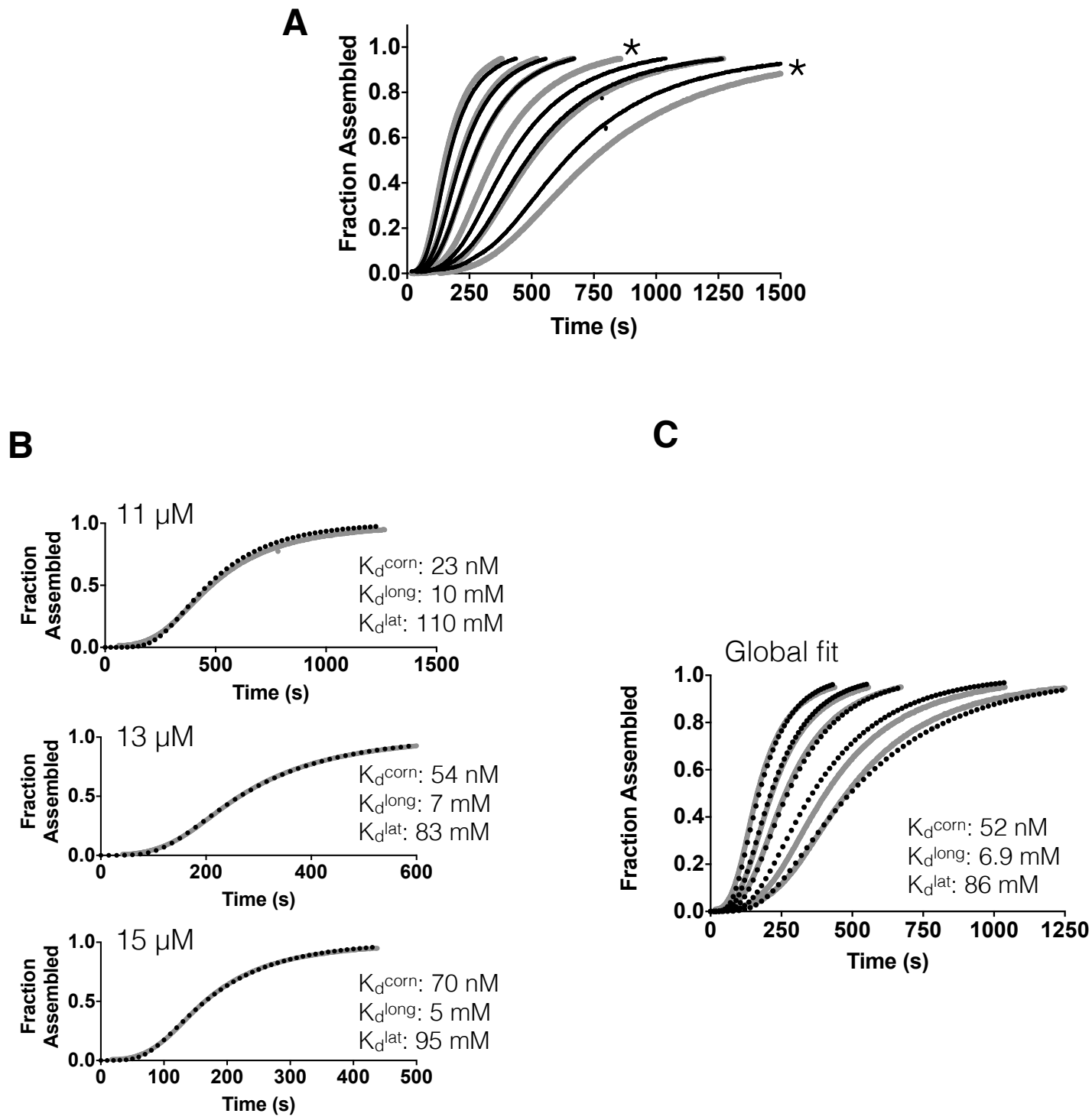

Supplemental Figure 3 Fit to an independent dataset

A Two independent data sets. The set plotted in grey is the one analyzed in the main text. The set in black was collected independently. Tubulin concentrations were 10, 11, 12, 13, 14, 15 μM for each. Most of the curves agree very closely, with the exception of two outlier curves (10 and 12 μM, indicated with # and *, respectively). The 10 μM curve was omitted from panel C.

B Fits of the layer model (black dotted line) to individual assembly curves (solid grey line) at different concentrations. Fits to individual curves are good. Inset text shows the resulting longitudinal, lateral, and 'corner' (simultaneous longitudinal and lateral interactions) affinities, which are within 10% of those obtained in the main text (see Fig. 2B).

C Global fit of the model (black dashed lines) to the alternate set of assembly data (grey lines). The model underestimates the concentration-dependence of the progress curves.

Illustration of the dimer pathway

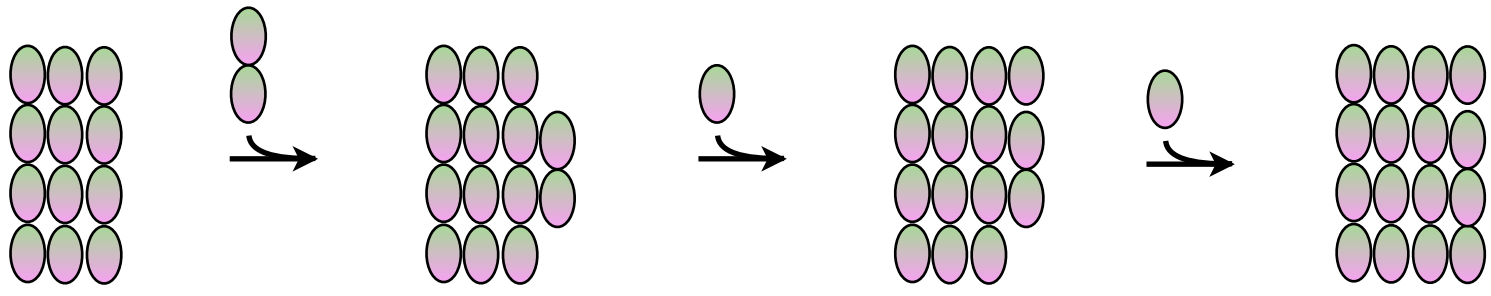

Initiation by lateral addition of a **longitudinal dimer**

'Zipping' of the layer by subsequent addition of **monomers**

Supplemental Figure 4 Illustration of the dimer pathway.
Cartoon sequence of steps for adding a new lateral layer. In the dimer pathway, a new lateral layer can be initiated by association of a pre-formed longitudinal dimer (left). Because the concentration of these longitudinal dimers of $\alpha\beta$-tubulin is much less than that of $\alpha\beta$-tubulin 'monomers', subsequent 'zipping' of the layer occurs by monomer addition. See Methods for a derivation of the equilibrium binding constant for the initiating assocition.

Supplemental Figure 5

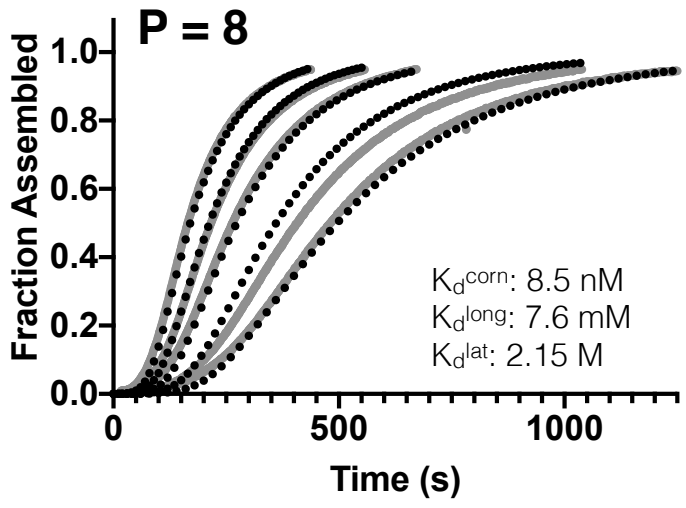

1202 **Supplemental Figure 5** Fit of the dimer+penalty model to an independent
1203 dataset
1204 Global fit of the dimer+penalty model (black dotted lines) to the alternate set of
1205 assembly data (grey lines). The global fit is good (with the exception of the 12 μM
1206 outlier curve noted in Sup. Fig. 3). The fitted parameters are close to those
1207 obtained from fitting to the original dataset, but for this dataset the corner affinity
1208 is ~1.4-fold stronger and the longitudinal affinity is ~1.3-fold weaker.
1209

Supplemental Figure 6

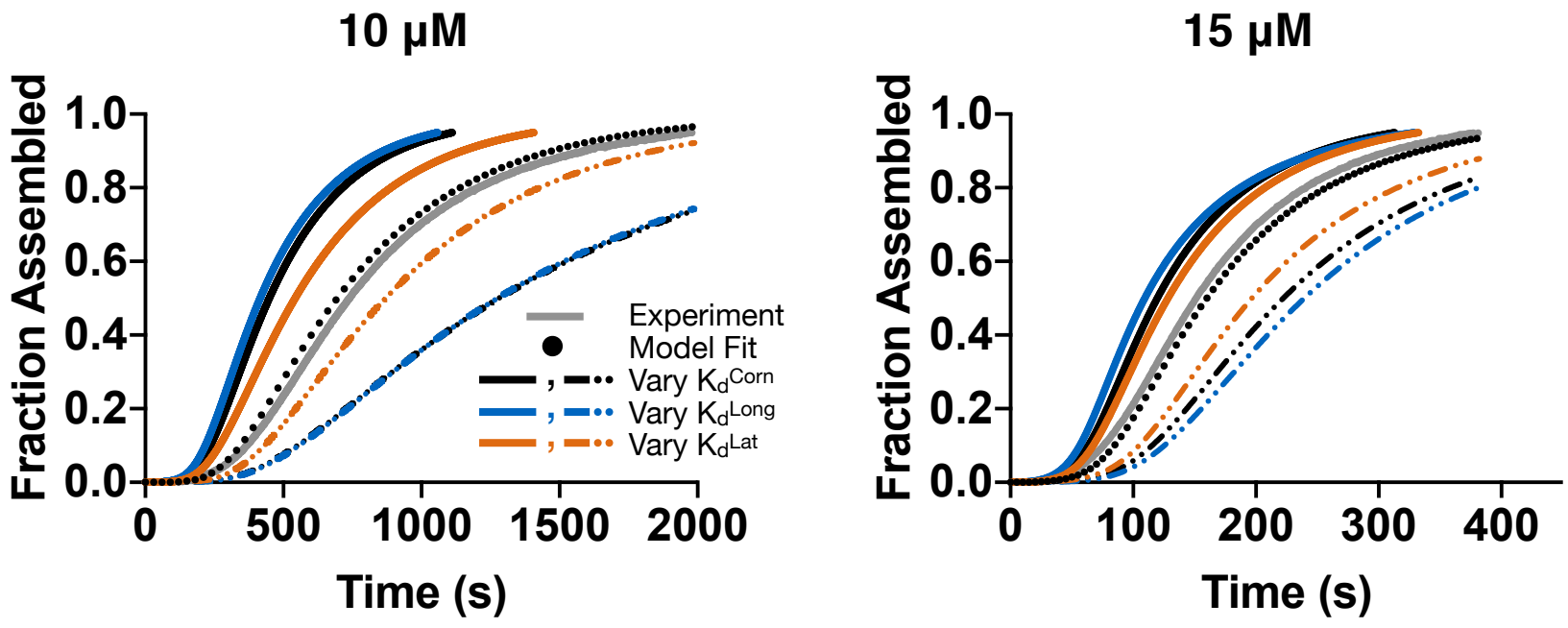

Supplemental Figure 6 Sensitivity of model predictions to variations in the underlying parameters.

The dimer+penalty model was run with individual affinities made stronger (solid lines) or weaker (dashed lines) by a factor of 1.5. Two different concentrations are illustrated. The model predictions are comparably sensitive to variation in corner (black) and longitudinal (blue) affinities, and less sensitive to variation in the lateral affinity (orange).

Supplemental Figure 7

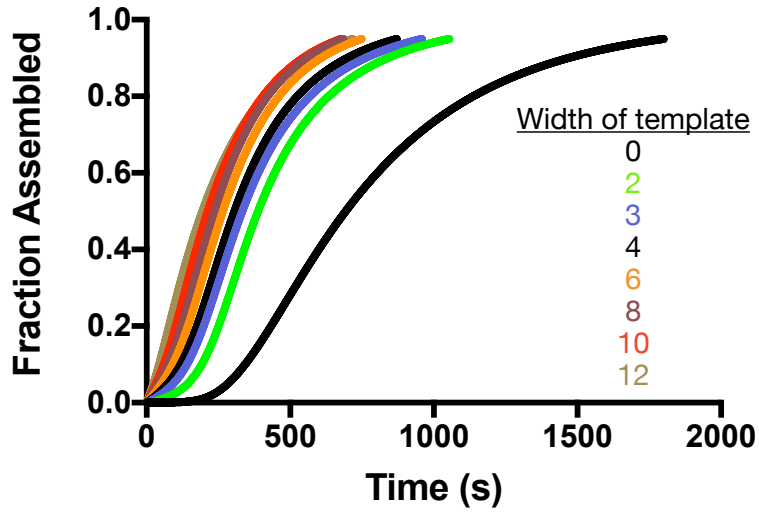

1217 **Supplemental Figure 7** Simulations of templated microtubule assembly.
1218 Simulated nucleation curves in the presence of γ-tubulin templates of different
1219 width assuming γ:$\alpha\beta$ interactions are the same strength as $\alpha\beta$:$\alpha\beta$ interactions.
1220 Compare to Fig. 6. The total concentration of templating monomers is held
1221 constant. Templates that are only two subunits wide (bright green) show much
1222 stronger nucleation than when we assumed weaker γ:$\alpha\beta$ interactions (compare
1223 green curve to the one in Fig. 6).
1224

Origin of the weighting factors used in the steady-state derivation (equations 5-8)

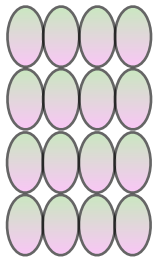

To initiate a new longitudinal layer, there are 8 (=2*width) different places for an αβ-tubulin to associate. This explains the factor of 8 in equation 5.

Two 'singleton' configurations present one corner site and two present two corner sites. On average there is 1.5 corner sites presented, hence the factor of 6/4 in equations 5 and 6.

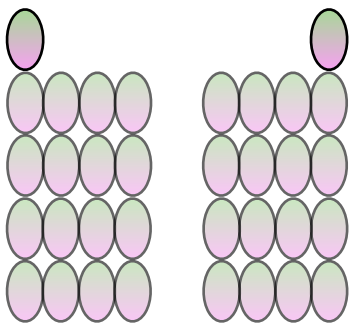

If the initiating αβ-tubulin is at the extreme left or extreme right, only 1 open corner site is presented.

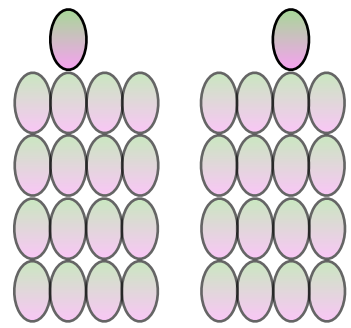

If the initiating αβ-tubulin is at either middle site, 2 open corner site are presented.

With two tubules added, two configurations present one corner site and one presents two corner sites. On average there is 1.33 corner sites, hence the factor of 4/3 in equations 6 and 7.

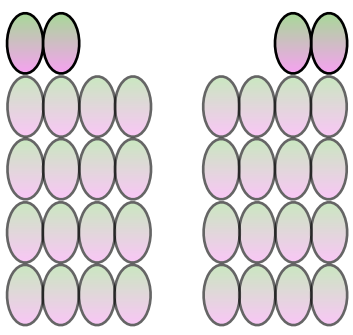

After the second addition, there are two configurations that present 1 open corner site

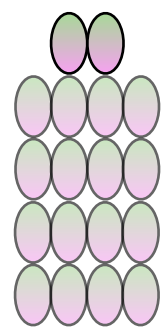

But there is only one configuration that presents two open corner sites

After the third addition, there are only two configurations that each present 1 open corner site. No weighting is applied.

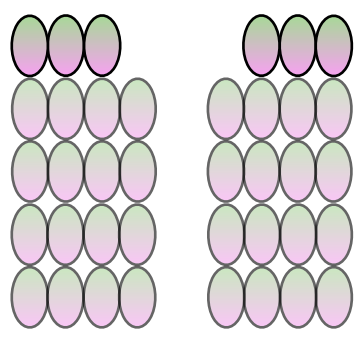

The explanations above explain the weighting factors on k_f in Equations 5, 6, and 7. Weights for a layer of size N can be similarly obtained from a general expression. For a layer of size n, the weights for the first, second, third, etc associations are: 2n, 2(n-1)/n, 2(n-2)/(n-1), etc.

Supplemental Figure 8 Derivation of kinetic weighting factors
Cartoons illustrating the sequence of intermediates for a ‘layer addition’, annotated to indicate the origin of the weighting factors applied in equations 5-8. Illustrations are made for the specific case of a layer of size 4, but the general expression for the coefficients is provided at the bottom of the figure.